Title

Mechanosensitive hormone signaling promotes mammary progenitor expansion and breast cancer risk.

Journal

Cell Stem Cell, 31(1)

Authors

Northey, Jason
Hayward, Mary-Kate
Yui, Yoshihiro
et al.

Publication Date

2024-01-04

DOI

10.1016/j.stem.2023.12.002

Peer reviewed

HHS Public Access

Author manuscript

Cell Stem Cell. Author manuscript; available in PMC 2025 January 04.

Published in final edited form as:

Cell Stem Cell. 2024 January 04; 31(1): 106–126.e13. doi:10.1016/j.stem.2023.12.002.

Mechanosensitive hormone signaling promotes mammary progenitor expansion and breast cancer risk

Jason J. Northey[1,2], **Mary-Kate Hayward**[1,2], **Yoshihiro Yui**[3], **Connor Stashko**[1,2], **FuiBoon Kai**[4,5], **Janna K. Mouw**[1,2], **Dhruv Thakar**[1,2], **Jonathon N. Lakins**[1,2], **Alastair J. Ironside**[6], **Susan Samson**[7], **Rita A. Mukhtar**[1], **E. Shelley Hwang**[8], **Valerie M Weaver**[1,2,7,9,10,*]

[1]Department of Surgery, University of California San Francisco, San Francisco, CA, 94143, USA

[2]Center for Bioengineering and Tissue Regeneration, University of California San Francisco, San Francisco, CA, 94143, USA

[3]Research Institute, Nozaki Tokushukai Hospital, Tanigawa 2-10-50, Daito, Osaka 574-0074, Japan

[4]Department of Physiology & Pharmacology, University of Calgary, Calgary, Alberta, T2N1N4, Canada

[5]Department of Biochemistry & Molecular Biology, University of Calgary, Calgary, Alberta, T2N1N4, Canada

[6]Department of Pathology, Western General Hospital, NHS Lothian, Edinburgh, EH42XU, UK

[7]UCSF Helen Diller Comprehensive Cancer Center, University of California San Francisco, San Francisco, CA, 94143, USA

[8]Department of Surgery, Duke University Medical Center, Durham, NC, 27710, USA

[9]Department of Bioengineering and Therapeutic Sciences, University of California San Francisco, San Francisco, CA, 94143, USA.

[10]Department of Radiation Oncology, Eli and Edythe Broad Center of Regeneration Medicine and Stem Cell Research, University of California San Francisco, San Francisco, CA, 94143, USA.

[*]**Lead Contact and Corresponding Author:** Valerie M. Weaver, Center for Bioengineering and Tissue Regeneration, Department of Surgery, University of California, San Francisco, valerie.weaver@ucsf.edu.

AUTHOR CONTRIBUTIONS

V.M.W. and J.J.N. conceived, designed and directed the study. J.J.N., F.K. and C.S. conducted AFM analysis. C.S. performed STIFMaps analyses. J.J.N. and M-K.H. performed H&E and IHC staining and qRT-PCR analysis of mammary tissues. A.J.I. assessed tissue pathology. J.J.N. and D.T. performed T47D and MCF7 hydrogel studies. Y.Y. completed initial $V737N^{M}$ mouse studies and J.J.N completed all other mouse studies. J.J.N. performed FACS, lineage tracing, colony formation and LDTAs. J.J.N. performed 3D hydrogel studies *in vitro* and *in vivo*. J.K.M participated in initial study design and analysis. J.N.L. designed and developed the $V737N^{M}$ mice and provided technical support. S.S. provided intellectual input and editorial input. R.A.M. and E.S.H. provided human specimens and patient data and contributed to clinical study design and analysis. V.M.W. and J.J.N. wrote the manuscript with editorial input from all authors.

DECLARATION OF INTERESTS

The authors declare no competing interests.

Summary:

Elevated mechanosignaling and matrix stiffness promote progesterone and RANK mediated expansion of mammary progenitors and breast cancer risk.

SUMMARY

Tissue stem-progenitor cell frequency has been implicated in tumor risk and progression, but tissue-specific factors linking these associations remain ill-defined. We observed that stiff breast tissue from women with high mammographic density, who exhibit increased lifetime risk for breast cancer, associates with abundant stem-progenitor epithelial cells. Using genetically engineered mouse models of elevated integrin mechanosignaling and collagen density, syngeneic manipulations, and spheroid models, we determined that a stiff matrix and high mechanosignaling increase mammary epithelial stem-progenitor cell frequency and enhance tumor initiation *in vivo*. Augmented tissue mechanics expand stemness by potentiating ERK activity to foster progesterone receptor-dependent RANK signaling. Consistently, we detected elevated phosphorylated ERK and progesterone receptor and increased levels of RANK signaling in stiff breast tissue from women with high mammographic density. The findings link fibrosis and mechanosignaling to stem-progenitor cell frequency and breast cancer risk, and causally implicate epidermal growth factor receptor-ERK-dependent hormone signaling in this phenotype.

eTOC BLURB

Weaver and colleagues uncover a role for integrin mechanosignaling in promoting mammary epithelial stem-progenitor cell frequency and fostering tumor initiation, and implicate mechanosensitive ERK-PR-induced RANK signaling in driving this process. Inhibiting these pathways could reduce cancer risk in women with high mammographic density.

Graphical Abstract

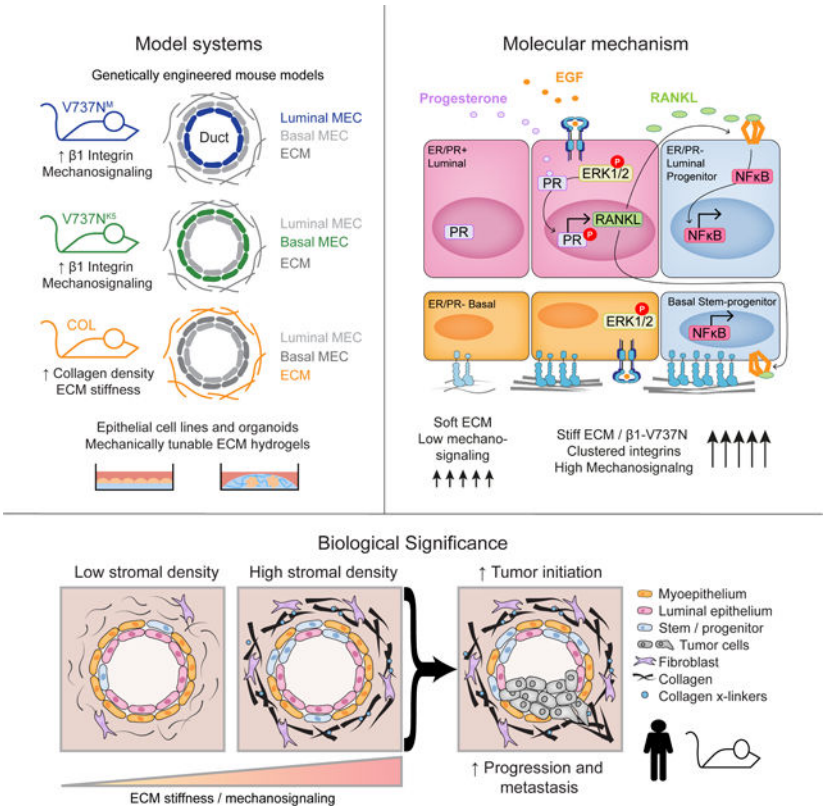

INTRODUCTION

The frequency of tissue stem-progenitor cells correlates with overall risk to malignancy.[1–3] Cancer stem cell frequency dictates tumor aggression, metastasis and treatment resistance.[4–8] Cancer stem cells may reflect expanded genetically modified resident stem cells or the trans-differentiation of tumor cells towards a stem-progenitor-like phenotype.[9,10] What tissue-specific factors regulate stem-progenitor cell frequency in tissues remain unclear.

The extracellular matrix (ECM) regulates the stem cell niche and its stiffness modulates cell growth, survival, tissue specific differentiation and tissue homeostasis.[9,11 12–15] The ECM is altered in tumors and higher grade tumors, which are usually metastatic with a high frequency of stem-progenitor cells, are the most fibrotic and stiff.[16–19] A stiff ECM promotes an epithelial-to-mesenchymal transition (EMT), and tumor cells that have undergone an EMT are enriched for the expression of stem-progenitor markers and exhibit stem-progenitor-like phenotypes[20–22]. Thus, tissue stiffness could modulate stem-progenitor cell frequency.

A stiff ECM modifies cell behavior by regulating cell signaling to influence gene expression.[9,11,23] A stiff ECM fosters the assembly of integrin focal adhesions which potentiate growth factor dependent extracellular signal-related kinase (ERK) and phosphatidylinositol 3−kinase (PI3K) signaling.[24–28] ECM stiffness also amplifies cytokine-stimulated G-Protein-Coupled Receptor (GPCR) activity,[14,19,29–31] permits morphogen-

induced Notch and Wnt activation[14,15,26] and facilitates β-catenin signaling.[32] Accordingly, we speculated that a stiff tissue could expand tissue-resident stem-progenitor frequency by altering the context of cell signaling. To test this, we studied the mammary gland which is a unique tissue that undergoes development in the adult organism where the growth, survival, invasion and differentiation of the mammary epithelium and stem-progenitor cells are tightly regulated by a circuit of hormones including estrogens, progesterone, and prolactin. Progesterone has been implicated in regulating stem-progenitor epithelial number in the breast.[33–35] Progesterone supplementation has also been linked to increased breast cancer risk in postmenopausal women,[36–40] and has been causally-associated with breast tumor progression in experimental models.[41–44] Indeed, estrogen, both stimulates progesterone receptor (PR) expression and regulates mammographic density (MD), with high MD conferring an elevated lifetime risk of breast cancer.[45–47] Moreover, high MD breast stroma is significantly stiffer than low MD breast stroma.[48,49]

We hypothesized that a stiff tissue regulates PR activity to expand the pool of normal mammary epithelial progenitors and that this in turn potentiates mammary tumor initiation and progression. We used transgenic and syngeneic mice, organoid models and clinical specimens to test this theory. Our studies revealed that a stiff ECM and elevated integrin mechanosignaling potentiate epidermal growth factor receptor (EGFR)-dependent ERK activity to promote progesterone-induced RANK signaling that expands the pool of mammary epithelial stem-progenitor cells. The findings suggest targeting either EGFR, ERK or RANK signaling might reduce breast cancer risk in women with high MD and have therapeutic implications for patients with highly fibrotic breast cancers.

RESULTS

High mammographic density associates with a mesenchymal phenotype and elevated mammary epithelial progenitor frequency

Women with high MD have a four-fold increased lifetime risk to malignancy, and their breasts contain more fibroglandular tissue.[48,50–52] We showed that the stroma of high MD tissue contains more fibrillar interstitial collagen and stromal fibroblasts that express higher levels of the collagen cross-linking enzymes lysyl oxidase (LOX) and lysyl hydroxylase 2 (LH2), and that their stroma is stiffer than that surrounding the ductal-lobular epithelium in low MD tissues (Figure 1A).[48] Given prior studies linking stem-progenitor frequency to cancer risk,[1–3] we examined the stiff, high MD tissue from premenopausal women for evidence of greater abundance of stem-progenitor mammary epithelial cells (MECs).

We utilized breast tissue classified as high and low MD from prophylactic mastectomy and performed FACS analysis to distinguish mature luminal (ML), luminal progenitor (LP) and basal MECs (Figure 1B, Table S1). We observed a striking increase in the relative abundance of the basal MEC compartment in tissues with high MD (Figure 1B), and colony formation assays indicated increased luminal and basal progenitor capacity (Figure 1C). IHC staining for ALDH, which associates with mammary epithelial progenitor activity, was also increased in the breast tissue isolated from women with high MD (Figure 1D). Given data linking a mesenchymal phenotype to epithelial stem-progenitor activity,[53–55] we next assayed the tissues for EMT markers. We noted that the average mRNA levels for several

mesenchymal genes including *SNAI1*, *VIM* and *FN1* were increased in tissues classified as high MD and correlated positively between patient samples (Figures 1E–1H). We then performed co-immunofluorescence staining of human breast tissue sections to visualize the collagenous ECM (CNA-35) together with the EMT and mammary epithelial progenitor associated proteins ZEB1 and SLUG.[20,56] Using Spatially Transformed Inferential Force Map (STIFMap), a machine learning approach that predicts stromal elasticity using collagen morphological features and ground truth elasticity measurements determined by Atomic Force microscopy (AFM),[55] we established a positive correlation between the predicted Young's modulus of the local breast tissue with epithelial cells marked by high levels of ZEB1 and SLUG (Figures 1I–1N). ZEB1 staining intensity also correlated positively with DAPI but not with collagen (CNA-35), while reverse associations were observed for SLUG illustrating that correlations with predicted elasticity do not depend solely upon DAPI or collagen staining alone. Indeed we have found that it is not always straightforward to relate an apparent collagen density to high stromal elasticity.[57,58] These data imply that women with high MD that have abundant regions of stiff breast stroma also have a higher frequency of epithelial stem-progenitor cells.

Mechanosignaling in luminal mammary epithelial cells promotes stem/progenitor-like activity

Activated β1-integrin levels were increased in the breast tissues of women with high MD, consistent with prior studies showing that ECM rigidity promotes focal adhesion assembly and integrin mechanosignaling (Figure 2A).[24–26] To investigate causality between ECM stiffness, integrin mechanosignaling and stem-progenitor MEC expansion, we engineered mice to conditionally express a mutant human β1-integrin (V737N) that promotes focal adhesion assembly and integrin signaling independent of cellular tension (Figure S1A).[26] V737N-β1-integrin transgene expression was targeted to MECs with MMTV-Cre, and using FACS and immunofluorescence staining to monitor transgene-coupled EGFP levels, we noted V737N-β1-integrin expression in both the luminal and basal compartments (Figures S1A–S1C). Co-immunofluorescence staining of mammary gland sections for PR, GFP, Keratin 8 and α-smooth muscle actin (α-SMA) showed a Cre recombination frequency of ~20–50% of total MECs with approximately 2-fold greater EGFP levels present in PR-positive and PR-negative luminal MECs compared to basal MECs (Figure S1D).

We next explored whether elevating integrin mechanosignaling could expand stem-progenitor frequency in the normal mammary gland (6- and 10-week-old $V737N^{M}$ and CTL^{M} mice; Figure 2B). Immunofluorescence staining for human β1-integrin, phospho-FAK and phospho-p130CAS demonstrated elevated levels in the MECs of $V737N^{M}$ mice, consistent with increased integrin mechanosignaling (Figures S1E–S1G).[26] Gross histological examination of the mammary glands of 6-week-old mice revealed an increase in the number and size of terminal end buds in $V737N^{M}$ mice (Figure 2C), as well as precocious primary, secondary, and tertiary ductal branching in 6- and 10-week old $V737N^{M}$ mice (Figures 2D and S1H). Proliferation (phosphor-Histone H3 immunofluorescence) was also elevated in the MECS of $V737N^{M}$ mice compared to CTL^{M} mice with higher proliferation increase for basal versus luminal MECs (Figures S1I–S1K). H&E-stained cross-sections of the $V737N^{M}$ mammary ducts revealed a thicker basal/myoepithelial

MEC layer (Figure 2E) that was confirmed by increased K14 immunofluorescence staining for lineage specific epithelial cytokeratins (Luminal, K8 and Basal, K14; Figure 2F). FACS analysis further demonstrated a higher ratio of basal-to-luminal MECs in $V737N^{M}$ mammary glands (Figure 2G), while co-immunofluorescence staining for PR, GFP, Keratin 8 and α-SMA demonstrated specific mechano-induced expansion of the basal MEC compartment (Figure S1L). The data suggest integrin mechanosignaling fosters the expansion of basal MECs.

To determine whether the higher frequency of basal MECs reflected an increase in stem-progenitor abundance, we used FACS to isolate luminal and basal MECS from CTL^{M} and $V737N^{M}$ mice and confirmed efficient sorting by gene expression for lineage specific markers (*Krt18*, *Krt5*; Figures S1M–S1N). Further qRT-PCR analysis revealed that the mesenchymal markers *Zeb1*, *Zeb2*, and *Snai1*, which have been implicated in basal stem-progenitor MECs,[59–62] were elevated in $V737N^{M}$ basal MECs as compared to CTL^{M} MECs, while levels of the luminal marker *Cdh1* remained largely unchanged (Figures 2H–2K). Given that putative mammary stem-progenitor cells reside within the basal MEC compartment, we next investigated whether mechanosignaling enhanced stem-progenitor MEC function by subjecting FACS-derived MECs to colony formation assays in reconstituted basement membrane (rBM) hydrogels. Although primary colony forming efficiency was unchanged between CTL^{M} and $V737N^{M}$ luminal and basal MECs (Figure 2L), the selective pressure for self-renewal following secondary colony formation revealed a significant increase in colony numbers for the $V737N^{M}$ basal MEC population and a corresponding decrease in $V737N^{M}$ luminal colonies (Figure 2M). Recent reports have defined populations of MEC progenitors with mixed lineage identity,[63–65] suggesting that $V737N^{M}$-derived luminal progenitors could have adopted a more basal progenitor-like fate. These effects were abolished when the mammary colonies were treated with a FAK inhibitor (FAKi; PND-1186) consistent with mechanosignaling-dependent stem-progenitor population self-renewal (Figure 2M). Limiting dilution transplantation assays (LDTAs), in which the ability of MEC populations to reconstitute the mammary gland is assessed by transplanting cell dilutions into the cleared fat pads of syngeneic mice, revealed a nearly 3-fold increase in stem-progenitor cell frequency for the $V737N^{M}$ basal MECs over CTL^{M} MECs, with more extensive epithelial outgrowth detected (Figure 2N–2P). The data demonstrate that luminal-directed integrin mechanosignaling fosters ductal proliferation and branching morphogenesis, concomitant with the expansion of basal-like stem-progenitor MECs.

A stiff collagenous stroma and elevated integrin mechanosignaling initiated in basal/myoepithelial cells promote stem/progenitor-like activity

The MMTV promoter is hormone responsive and directs transgene expression preferentially to luminal MECs, which are principally shielded from ECM interactions by a layer of basal/myoepithelial cells. To assess the impact of mechanosignaling in myoepithelial cells and elevated matrix density on MEC stem-progenitor phenotype, we employed mice engineered to conditionally express V737N-β1-integrin specifically in myoepithelial cells ($V737N^{K5}$), and mice that ubiquitously express a collagenase resistant mutant of collagen I (COL) that increases collagen density, stromal stiffness and integrin signaling (Figures 3A and 3B).[66–69]

Similar to observations in $V737N^{M}$ mice, immunofluorescence staining as well as FACS analysis revealed a notable shift in the luminal:basal MEC ratio that favored an increase in the abundance of the basal epithelium in both the $V737N^{K5}$ and COL mouse models (Figures 3C–3F). Co-immunofluorescence staining for MEC lineage specific markers with PR and EGFP corroborated an expansion of basal MECs without changes in the proportion of PR-positive luminal MECs in either the $V737N^{K5}$ or COL mice as compared to their corresponding control mice (Figures S2A–S2B). Notably, $V737N^{K5}$ glands exhibited ~2-fold greater EGFP expression (V737N) in basal MECs in contrast to $V737N^{M}$ mice (Figure S2C). Subsequent qRT-PCR analysis of FACS-derived MEC populations for epithelial specific markers (*Krt18*, *Krt5*) confirmed efficient sorting of MEC populations (Figures S2D–S2G) and revealed that several stem-progenitor-associated genes including *Snai2*, *Zeb1* and *Smarca2* were significantly upregulated in the basal compartment, while *Sox9* was highest in the luminal compartment of $V737N^{K5}$ and COL mice as compared to CTL^{K5} and WT mice respectively (Figures 3G–3N). These findings indicate that increasing collagen density and stromal stiffness or directly elevating mechanosignaling in basal MECs expands the basal epithelium and may endow MECs with enhanced stem-progenitor-like activity.

SLUG and SOX9 confer stem-progenitor cell activity and ZEB1 and SMARCA2 (a component of the SWI/SNF chromatin remodeling complex), interact with the mechanotransducers YAP/TAZ to promote basal MEC lineage fate and stem-progenitor cell maintenance.[20,60,70] To implicate these factors in mechanosignaling and ECM stiffness induced stem-progenitor cell abundance, we co-stained mammary sections from WT and COL mice for SLUG and ZEB1 together with collagen (CNA-35) to correlate their levels with stromal elasticity using STIFMap. STIFMap analysis demonstrated a substantial positive correlation for both ZEB1 and SLUG with predicted stromal elasticity in the WT and COL mammary glands that could not be accounted for by DAPI or collagen staining intensity alone (Figure S2H–S2L). These results agree with those obtained using human patient specimens (Figure 1I–1N) and further implicate ECM stiffness in driving the expansion of basal stem-progenitor MECs in these murine models.

LDTAs were used to test for a functional increase in mammary stem-progenitor cell activity in the basal epithelium of both the $V737N^{K5}$ and COL mammary glands. Consistently, basal MEC V737N expression resulted in a ~3-fold increase in stem-progenitor frequency (Figure 3O–3P), while increased collagen density promoted basal MEC stem-progenitor frequency by more than 4-fold (Figure 3Q–3R). In both instances, the overall extent of mammary repopulation was slightly greater, implying enhanced progenitor activity (Figure S2M–S2N).

To further test the impact of mechanosignaling on stem-progenitor cell frequency, we used a lineage tracing strategy to examine epithelial dynamics and clonal diversity during branching morphogenesis.[71] Tamoxifen induced activation of V737N-expression with fluorescent tagging of MEC clones for lineage tracing over 2-weeks displayed little differences in clonal frequency or size (number of cells/clone), with the exception of a modest increase in the frequency of multicellular clones in V737N-expressing glands (Figures S2O and S2P). However, a significant increase in clonal frequency was observed at 16 weeks post tamoxifen induction in the mammary glands of $V737N^{K5}$ mice as compared to CTL^{K5} mice (Figure 3S), indicating an expansion of basal MEC progenitor

activity contributing to ductal development in V737N^{K5} glands. CTL^{K5} mammary glands showed a reduction in single cell clones over time while single cell clones persisted in the mammary glands of V737N^{K5} mice, suggesting extended maintenance of their stem-progenitor phenotype (Figure 3S). The data indicate that stromal density and stiffness and elevated mechanosignaling support the expansion and activity of basal stem-progenitor MECs.

RANKL is required for mechanosignaling induced mammary stem-progenitor cell expansion

In the mammary gland, estrogens and progesterone modulate MEC proliferation and progenitor cell expansion.[33–35] To investigate the interplay between mechanosignaling and hormone-dependent stem-progenitor MEC expansion, we used FACS to isolate MECS from CTL^{M} and V737^{M} mice in diestrus (confirmed by vaginal cytology; Figure 4A)[72]. Analysis of EMT/stem-progenitor cell associated gene expression showed increases in *Smarca2*, *Sox9*, *Wwtr1 (Taz)*, *Yap1*, *Ctnnb1* and *Myc* in V737N^{M} versus CTL^{M} basal MECs (Figures 4B–4G), which we failed to uncover using MECs harvested from mice at mixed stages of the estrus cycle (Figures S2Q–S2V). These findings are consistent with tension-dependent regulation of stem-progenitor cells because YAP/TAZ, Smarca2 and Zeb1 collaboratively direct the basal MEC lineage and maintain mammary stem cell levels, and Wnt/β-catenin signaling and MYC induction in basal MECs is required for proficient MEC stem-progenitor activity.[60,70,73]

After demonstrating no detectable changes in transcript levels for the estrogen or progesterone receptors (*Esr1*, *Pgr (A and B)*, *Pgr (B)*) (Figures S3A–S3C), we examined the impact of the progesterone-induced paracrine factors, RANKL and WNT4, which regulate stem-progenitor MEC activity (Figure 4H).[33,34,74] ELISA revealed higher RANKL protein levels in mammary glands excised from V737N^{M} mice (Figure 4I). We also detected significantly higher gene expression for *Tnfsf11* (*Rankl*) in V737N^{M} luminal MECs that was confirmed at the protein level using immunofluorescence analysis (Figures 4J and 4K), as well as similar evidence for elevated *Tnfrsf11a* (*Rank*) transcript and RANK protein levels in luminal and basal V737N^{M} MECs (Figures S3D and S3E). Consistent with RANKL-induced proliferation, the cell cycle associated transcript *Ccnd1* was highly expressed in luminal V737N^{M} MECs compared to their corresponding CTL^{M} MECs (Figure 4L), and a modest increase in *Ccnd2* transcript was documented in V737N^{M} mouse-derived basal MECs (Figure S3F)[33]. Although *Wnt4* transcript levels were not increased in the V737N^{M} luminal MECs, gene expression for the Wnt signaling regulator R-SPONDIN1 (*Rspo1*) was elevated, in agreement with its recently described role in amplifying RANK-dependent signaling (Figure 4M and S3G).[75]

Evidence for associations between RANK signaling and integrin mechanosignaling, in the absence of large variability in estrogen or progesterone receptor levels (Figure S3H–S3M), were further confirmed in two additional mouse models, the V737N^{K5} (basal MEC mechanosignaling) and COL (increased collagen density/stromal tension) mice. In both mouse models, similar increases in RANKL/RANK gene and protein expression, and evidence for RANKL signaling induced MEC proliferation that included elevated

Ccnd1 and *Ccnd2* transcript levels, were detected using qRT-PCR and immunofluorescence analysis (Figures 4N and 4O and S3N–S3W). In contrast to findings in the MECs from $V737N^{M}$ mice, *Wnt4* but not *Rspo1* transcript levels were elevated in the luminal MECs of $V737N^{K5}$ mice, whereas neither transcript was elevated in the MECs from COL mouse mammary glands (Figures S3X–S3AA). These results provide additional evidence that tissue tension and integrin mechanosignaling enhance the frequency of stem-progenitor MECs and implicate progesterone-stimulated paracrine factors such as RANKL.

To causally implicate RANKL in mechanosignaling-induced stem-progenitor MEC expansion, cohorts of $V737N^{M}$ and COL mice with their controls were treated with a RANKL inhibitor (RANK:Fc) or murine:Fc (Mu:Fc) prior to basal MEC isolation and LDTA assessment. FACS analysis of luminal:basal MEC ratios confirmed that RANK:Fc treatment eliminated a large proportion of the basal MEC population in $V737N^{M}$ mammary glands (Figure 4P). LDTA confirmed that RANK:Fc treatment reduced stem-progenitor frequency and activity in the basal MECs isolated from both $V737N^{M}$ and COL mice towards that demonstrated by CTL^{M} and WT mice (Figures 4Q–4V). These data imply that integrin mechanosignaling, induced either through genetic manipulation or by increased stromal density and stiffness, drives stem-progenitor MEC expansion and implicate RANKL signaling in this phenotype.

Progesterone receptor activity is augmented by mechanosignaling

PR activity is modulated through post-translational phosphorylation of several residues including ERK-dependent phosphorylation on Serine 294 (S294) that enhances PR transcription and increases the expression of genes associated with stem-like tumor cells (Figure 5A).[76,77–80] Immunoblot analysis revealed a consistent and notable increase in the levels of phospho-ERK and phospho-PR (S294) as well as elevated nuclear p65-NFκB in the luminal MECs isolated by FACS from $V737N^{M}$ mice when compared to those isolated from CTL^{M} mice (Figures 5B and 5C). These data imply that a stiff ECM and elevated mechanosignaling could modify PR transcriptional activity through its tension-dependent ERK-mediated phosphorylation that subsequently enhances RANK signaling.[24,81]

To directly test whether ECM stiffness/mechanosignaling could enhance ERK-dependent PR phosphorylation at S294, PR-expressing T47D and MCF7 breast cancer cells were cultured on “SOFT” (400 Pascals) and “STIFF” (60 kPa) fibronectin coated polyacrylamide gels to represent ECM elasticities typical of normal mammary stroma or fibrotic mammary tumors.[17,48,82] Immunoblot analysis revealed that a stiff ECM synergistically enhanced the ability of the PR-agonist promegestone/R5020 and epidermal growth factor (EGF) to stimulate S294 phosphorylation of PR (Figures 5D–5F and S4A–S4C).

Immunofluorescence staining of freshly isolated mammary organoids from CTL^{M} and $V737N^{M}$ mice cultured within collagen-I/rBM hydrogels (Col1/rBM) to generate “STIFF” (Lribose cross-linked; ~1700 Pascals) and “SOFT” (~600 Pascals) ECMs demonstrated significantly greater nuclear translocation of PR in EGF/R5020-treated CTL^{M} organoids embedded within the STIFF ECM, as well as in the EGF/R5020-treated $V737N^{M}$ organoids within the SOFT ECM, compared to their non-treated controls or the CTL^{M} organoids in the SOFT ECM regardless of EGF/R5020 stimulation (Figure S4D).[25,48,83] Subsequent gene

expression analysis revealed that EGF/R5020-treated CTL^M organoids within the STIFF ECM and treated V737N-β1-integrin expressing organoids within the SOFT ECM expressed higher levels of *Tnfsf11* (*Rankl*) versus CTL^M organoids in the SOFT ECM (Figure S4E). An ELISA of conditioned media from these cultures confirmed similarly elevated protein levels of RANKL, without ECM stiffness dependent influence over luminal MEC number as assessed by transcript levels for the luminal MEC marker Krt18 (Figure S4F and S4G). Importantly, treatment of mammary organoids with a FAKi or an EGFR inhibitor (EGFRi; Tyrphostin/AG-1478) abrogated ECM stiffness and mechanosignaling induced RANKL levels (Figures S4E and S4F).

Immunofluorescence staining of mammary tissue from $V737N^M$, $V737N^{K5}$ and COL mice demonstrated elevated nuclear pPR-S294 and p65-NFκB compared to their controls (Figures 5G–5L). Consistently, immunoblot analysis of nuclear lysates from whole mammary glands of these mouse models revealed $V737N^M$ and COL mammary glands had markedly higher levels of pPR-S294 versus CTL^M and WT glands, with modest elevations quantified between $V737N^{K5}$ and CTL^{K5} glands (Figure S4H and S4I). Using the same analysis, nuclear p65-NFκB levels were found to be elevated in all mouse models with increased mechanosignaling/stromal stiffness (Figure S4H and S4J), consistent with tension-dependent increases in RANKL signaling.

The relevance of the elevated phospho-ERK activity detected in all three of the mouse models with elevated mechanosignaling/stromal stiffness (Figure S5A–S5C) to RANK-dependent stem-progenitor cell expansion was verified by showing that $V737N^M$ mice treated with an ERK inhibitor (ERKi; Temeturkib) had abrogated MEC p65-NFκB nuclear localization (Figure S5D–S5F), and reduced basal MEC stem-progenitor activity as indicated by LDTA (Figures 5M–5O). These data support a role for ECM stiffness/mechanosignaling in potentiating progesterone-induced RANKL signaling in MECs, and suggest that this phenotype is mediated through enhanced ERK-mediated phosphorylation of PR.

Tissues with high mammographic density exhibit elevated ERK and progesterone/RANK signaling

We next examined whether tension-dependent integrin-EGFR-ERK-induced progesterone-RANK signaling could explain the higher frequency of stem-progenitor MECs detected in the breast tissue of patients with high MD (Figure 1). Immunofluorescence analysis revealed that MECs within high MD tissue had higher levels of phospho-ERK and phospho-PR (S294) (Figures 6A and 6B), and qRT-PCR uncovered elevated *TNSFS11 (RANKL)* levels that immunofluorescence showed translated to higher RANKL protein (Figures 6C and 6D). Gene expression levels for the RANKL decoy receptor, *TNFRSF11B (OPG)*, and *TNFRSF11A (RANK)* were similar between the high and low MD tissues (Figures 6E and 6F); however, immunofluorescence staining indicated RANK protein and nuclear p65-NFkB levels were increased in a manner consistent with increased RANK activity in high MD tissues (Figure 6G and 6H). A correlation matrix comparing immunofluorescence within the same patient tissue for active β1-integrin (Figure 2A), pPR-S294 (Figure 6B) and RANKL (Figure 6D) uncovered a positive correlation between these factors and RANKL (Figure 6I).

To decrease potential variability linked to systemic progesterone, we compared the RANKL levels from regions of the same breast classified as high and low MD and quantified by AFM as stiff and soft, respectively (Figure 6J). *TNSFS11* (*RANKL*) levels and stromal stiffness correlated significantly among the 4 patients examined as indicated by similar slopes between the lines linking levels of each parameter between the two regions tested (Figure 6K). These findings link elevated lifetime risk for breast cancer in women with high MD with stem-progenitor MEC frequency and implicate stiffness-enhanced, EGFR-ERK-dependent progesterone-induction of RANKL and elevated RANK signaling in this phenotype.

Tissue tension promotes premalignant and early malignant lesion formation

Given our observations that stromal stiffness/mechanosignaling can foster progesterone/RANKL induced stem-progenitor expansion in the normal mammary gland, we postulated that this would drive mammary tumor risk and early epithelial lesion formation. Because preneoplastic and early neoplastic lesions in the mammary gland typically retain estrogen and progesterone signaling, we opted to assess the impact of activated MEC integrin mechanosignaling and stromal stiffness on early tumor lesion formation.[84–86] We utilized $V737N^{Neu}$ and Neu mice, and furthermore crossed the $V737N^{K5}$ and COL mice with MMTV-PyMT mice (Figures 7A–7C), for examination at an appropriate early time point characterized by the presence of premalignant and early malignant lesions. These analyses revealed a trend toward an increased frequency of epithelial hyperplasia and early-stage tumor lesions in $V737N^{Neu}$ cohorts compared to Neu control mice (Figure 7D). Mechanosignaling in basal MECs (K5-$V737N^{PYMT}$) and elevated stromal stiffness (COL^{PyMT}) resulted in a clear elevation of early and premalignant epithelial lesion formation (Figures 7E and 7F).

Inhibiting RANKL signaling with RANK:Fc prevented the expansion of stem-progenitor MECs in the normal murine mammary gland. To implicate mechanosensitive ERK-PR induced RANKL signaling in early lesion formation, we treated $V737N^{Neu}$ and COL^{PyMT} mice and their corresponding controls with either murine:Fc or RANK:Fc prior to mouse sacrifice at the indicated time points. In all cohorts, RANK:Fc treatment diminished early lesion formation but achieved the most significant reduction in $V737N^{Neu}$ and COL^{PyMT} mice (Figure 7G and 7H). Nuclear p65-NFκB levels were also reduced in the RANK:Fc treated $V737N^{Neu}$ mice, providing evidence of treatment specificity (Figure 7I). These data suggest RANKL blockade could be applied to prevent tumor progression in patients with preinvasive breast cancer (DCIS) or precursor lesions and could reduce risk where there is evidence of high collagen density and integrin mechanosignaling.

Tissue tension promotes a mesenchymal tumor cell phenotype and lung metastasis

Tissue fibrosis associates with breast cancer aggression. Fibrotic tumors have increased ECM cross-linking that stiffens the stroma and elevates tumor cell integrin mechanosignaling and EGFR-dependent ERK activity.[16–18,87] A stiff ECM also drives a mesenchymal-like invasive phenotype and metastatic behavior in tumor cells.[25,26,88–90] Thus, elevated mechanosignaling could drive tumor aggression by enhancing stem-progenitor frequency. We examined the impact of enhanced integrin mechanosignaling on

tumor progression by monitoring V737N^{Neu} mice (Figure S6A) to experimental endpoint as defined by maximum tumor volume, and simultaneously documented tumor latency, phenotype and metastasis as compared to age-matched Neu mice. Immunofluorescence imaging indicated enhanced mechanosignaling in V737N^{Neu} tumors, as phospho-ERK, phospho-FAK (Y397) and active β1-integrin levels were all increased (Figures S6B–S6D).[26] However, tumor latency did not appreciably differ between Neu and V737N^{Neu} mice (Figure S6E), and we failed to observe differences in the rate of tumor outgrowth and tumor cell proliferation (phospho-Histone H3) or viability (cleaved Caspase-3) (Figures S6F–S6H). Nevertheless, the incidence of lung metastasis was profoundly increased in V737N^{Neu} mice (Figure S6I) with a 7-fold increase in the average number of lung lesions per animal (Figure S6J). Lung lesions in V737N^{Neu} mice were also significantly larger than those in Neu mice (Figure S6K). The findings suggest qualitative differences in the nature of the tumors that developed in the V737N^{Neu} mice, consistent with an impact on stem-progenitor MEC frequency.

To assess the impact of integrin mechanosignaling on tumor phenotype, we examined the histology of tumors in Neu and V737N^{Neu} mice. We noted that a higher proportion of V737N^{Neu} mice developed dense, highly packed tumors lacking luminal space, and displayed features consistent with an aggressive phenotype, such as increased nuclear pleomorphism, increased nuclear crowding and conspicuous mitotic activity when compared to Neu mice (Table S2, Figure S6L). V737N^{Neu} tumors expressed higher transcript levels for several mesenchymal genes including *Snai1*, *Snai2* (p=0.083), *Fn1* (p=0.084) and *Vim* (Figures S6M–S6P). IHC and immunofluorescence for the luminal epithelial markers, E-Cadherin and ERα, in V737N^{Neu} tumors demonstrated decreased protein expression that aligned with qRT-PCR analysis of their corresponding mRNAs (Figures S6Q–S6T). Interestingly, there was also an almost two-fold increase in tumor multiplicity in the V737N^{Neu} mice, suggesting elevated mechanosignaling could enhance the potential for tumor initiation; a finding in support of a stem-progenitor cell phenotype (Figure S6U). Consistently, FACS analysis revealed a greater abundance of a CD24^{+}CD49^{hi}CD61^{hi} tumor initiating cell (TIC) population in V737N^{Neu} versus Neu tumors (Figure 6SV).[55] These data indicate that increased mechanosignaling cultivates a mesenchymal/stem-like cell phenotype that enhances the ability of mammary tumor cells to metastasize and might additionally foster tumor initiation.

To directly test whether a fibrotic ECM could promote a stem-like TIC phenotype, we embedded MMTV-PyMT mouse derived tumor cells into the fat pads of syngeneic mice within SOFT and STIFF Col1/rBM ECM hydrogels (Figure S7A).[25,83] Immunofluorescence for phosphor-ERK, phospho-FAK and active β1-integrin demonstrated increased mechanosignaling in tumor cells implanted within the STIFF ECM stroma; without significantly impacting tumor growth rates (Figures S7B–S7E). Picrosirius red imaging of mammary glands inoculated with the SOFT and STIFF Col1/rBM ECM at 4 weeks post injection verified collagen density differences were maintained (Figure S7F), and immunoblot analysis revealed that total ERK and FAK levels were unaltered by increased stromal stiffness *in vivo* (Figure S7G). PyMT tumors in the STIFF ECM stroma gave rise to a higher percentage of mice presenting lung metastases with a larger average size (Figures S7H–S7J). IHC staining of lung metastases for phospho-Histone H3 and

cleaved Caspase-3 revealed no apparent differences in proliferation and survival between metastatic cells originating from tumors with SOFT and STIFF ECM stroma, suggesting that a selective growth advantage at the secondary site could not account for the observed STIFF ECM enhanced metastasis (Figures S7K and S7L). Instead, qRT-PCR analysis of primary tumors demonstrated that STIFF tumors showed increased expression of the mesenchymal gene, *Snai2*, and lower levels of the epithelial marker *Cdh1* (Figures S7M and S7N). STIFF ECM conditioned tumor cells also demonstrated greater tumor initiating potential as assessed by limiting dilution tumorigenesis assays in comparison to their SOFT ECM derived counterparts (Figures S7O). FACS analysis of tumor cells isolated from the SOFT and STIFF ECM stroma further suggested an increased frequency of TICs in tumors with STIFF ECM stroma (Figure S7P). These data extend and reinforce prior observations that a stiff, fibrotic ECM and elevated mechanosignaling induce a mesenchymal phenotypic shift in tumor cells.[55] Our data further suggest that a stiff ECM can foster progenitor cell-like properties in both normal and malignant settings and that this mechanism has implications for both tumor initiation and the origin of aggressive tumor phenotypes.

DISCUSSION

Our findings highlight the critical role played by mechanical cues in regulating stem-progenitor cell frequency and are consistent with prior data implicating ECM stiffness in stem-progenitor cell proliferation and viability.[12,14,15,91–94] Here we identified a molecular mechanism whereby a stiff ECM increases stem-progenitor cell frequency through the tension-dependent enhancement of β1-integrin mechanosignaling that drives EGFR-dependent ERK activity, and potentiates progesterone induced RANKL-RANK activity. Our results provide an explanation for why deleting β1-integrin in the basal MEC population reduced basal progenitor activity to favor luminal differentiation,[95] and why deleting FAK in the entire breast epithelium so potently impaired luminal and basal progenitor cell function.[96] Given that basal-like luminal progenitor cells or mixed lineage basal-luminal alveolar cells were recently characterized in human breast tissues and that HER2-positive and basal-like human breast cancers are thought to originate from luminal progenitor MEC populations,[65,97,98] this suggests β1-integrin mechanosignaling favors the emergence of aggressive breast cancer subtypes by expanding a pool of basal-like MEC progenitors.

Conceptually our findings are consistent with earlier work illustrating how a stiff ECM potentiates cell growth and survival by enhancing the context of growth factor receptor and GPCR signaling, but critically expand this paradigm to include modification of hormonal signaling and transcription.[14,19,24–31] We demonstrate that ECM stiffness and mechanosignaling modulate PR signaling, progenitor-like MEC function and a mesenchymal breast cancer phenotype. Our data are consistent with reports that ECM remodeling through ovarian hormones induces ADAMTS18 which is important for the maintenance of mammary progenitor cells via Hippo and Wnt signaling.[99] We also showed that mechanosignaling disrupts membrane β-catenin localization in MECs,[26] which is indicative of active Wnt signaling and in agreement with observations that PRinduced RANKL/WNT4 can foster early dissemination of HER2-induced mammary tumor cells.[100] Our studies mechanistically link stromal stiffness/mechanosignaling to epithelial progenitor expansion by demonstrating that these factors potentiate ERK-mediated PR phosphorylation

at S294, which has been associated with enhanced cancer stem cell associated gene expression in breast cancer.[79] Our findings thereby suggest that interventions aimed at reducing stromal stiffness or blocking this PR-sensitive mechanistic pathway could prevent tumor initiation and progression.

The highly fibrotic breast cancer subtypes have elevated RANK expression.[101] Recent reports showed that tissues from women with a BRCA1 mutation express high levels of RANK and harbor a higher frequency of progenitor-like cells, and that tissues with high MD have elevated RANKL expression.[101–104] RANK signaling can promote an EMT in normal MECs and in breast cancer cells.[86,105] Our data suggest that risk factors that contribute to tumor initiation may be functionally-linked to a stiffer stroma and elevated mechanosignaling. Not only did we observe more RANKL and RANK in high MD tissues and mechanically activated mouse mammary tissue, but we also observed elevated levels of nuclear p65-NFκB. Nuclear “active” NFκB will induce cytokine expression to drive inflammation and alter anti-tumor immunity. Indeed, women with high MD have more infiltrating myeloid cells, and TNBCs typically have a stiffer stroma characterized by a high density of infiltrating inflammatory myeloid cells.[17,106] Several immune populations produce and respond to RANKL,[107] and FoxP3-positive regulatory T cell (Treg)-derived RANKL promotes RANK-positive tumor cell metastasis in breast cancer.[108] Treg cells may be recruited by αSMA-positive fibroblasts in fibrotic tumor stroma, and Treg cells could thereafter drive tumor progression and stem-progenitor cell expansion by secreting RANKL and enhancing the recruitment of myeloid cells through NFκB activation and elevated cytokine expression. Indeed, RANKL inhibition limits tumor progression by improving CD8-positive T cell responses alone and in combination with immune checkpoint inhibitors.[109–111] Our findings provide new evidence supporting the use of RANKL inhibition as an anti-cancer treatment and as a prevention modality, particularly in individuals with a stiffer stroma and more integrin mechanosignaling, such as those with high MD. These findings have stimulated recent clinical trials testing the RANKL inhibitor Denosumab as an agent to improve outcomes for patients with early breast cancer and to reduce risk in patients with high MD (ClinicalTrials.gov: NCT03691311 D-BIOMARK, and NCT04067726 TRIDENT).

LIMITATIONS of the STUDY

The clinical data is limited by specimen availability and clinical parameters. We focused on premenopausal women without known BRCA1 mutation to avoid complicating variables. Due to limited patient numbers, we did not address additional factors such as age, race, BRCA1 mutation and postmenopausal status. Potential variability could be related to differences in genetic backgrounds of murine models and tamoxifen-inducible-Cre for conditional transgene expression. All murine models were maintained on pure FVB/NJ genetic backgrounds with the exception of the $V737N^{K5}$ and CTL^{K5} mice, which were maintained on a pure C57Bl/6J background. Note: C57Bl/6J mice are more resistant than FVB/NJ mice to mammary tumor progression and have subtle differences in the magnitude and complexion of MEC response to ovarian hormone signaling.[112,113] These mice also use a Keratin 5-promoter driven tamoxifen-inducible-Cre for transgene expression and the ER antagonist tamoxifen can delay mammary gland ductal development. To circumvent

these issues, we used later time points to analyze these mice in study comparisons. Further limitations arise from the inherent heterogeneity and dynamic nature of MEC populations that future studies could address using single cell RNA sequencing.

STAR METHODS

RESOURCE AVAILABILITY

Lead Contact—Further information and requests for resources and reagents should be directed to and will be fulfilled by the lead contact, Valerie M. Weaver (valerie.weaver@ucsf.edu).

Materials Availability—This study did not generate any new unique reagents.

Data and Code Availability—The authors declare that all data supporting the findings of this study are available within this publication and its supplemental data. Original western blot images and FACS gating strategies have been deposited at Mendeley Data and are publicly available as of the date of publication. The DOI is listed in the key resources table (doi: 10.17632/phrmytzyss.1). Microscopy data reported in this paper will be shared by the lead contact upon request. Any code used in the preparation of this manuscript is publicly available from software and commercial sources. All original code necessary to implement STIFMaps has been deposited and is publicly available via the Github repository https://github.com/cstashko/STIFMaps. Any additional information required to reanalyze the data reported in this paper is available from the lead contact upon request.

EXPERIMENTAL MODEL AND STUDY PARTICIPANT DETAILS

Human Study Participants, Breast Tissue Collection and Processing—For tissue analyses, all patients were female and nearly all were premenopausal with no other selection bias based on age, race or ethnicity. Normal human breast tissues were surgical resection of breast reduction or prophylactic mastectomies. Tissue specimens were collected from prophylactic mastectomy and 2×2 cm pieces were formalin-fixed and paraffin embedded (FFPE), or flash frozen in OCT (Tissue-Tek) by slow immersion in liquid nitrogen or placement on dry ice. Similarly sized fragments were also collected as fresh tissue with immersion in media (phenol red free-DMEM/F12) with 10% charcoal stripped fetal bovine serum (FBS Benchmark, Cat. #: 100–106) and GlutaMAX (Gibco, Cat. #: 35050–061) supplementation for transportation to the Weaver laboratory at UCSF. Fresh tissue was used for FACS-mediated human MEC isolation and subsequent culture in colony formation assays or for RNA extraction. All human breast tissue specimens were collected prospectively from consenting patients (informed consent provided prior to surgery) undergoing surgery at the University of California, San Francisco, (UCSF) or Duke University Medical Center between 2010 and 2020. Premenopausal women were selected prior to surgery and approached by surgical teams to give informed consent for tissue collection. Samples were collected, stored and analyzed with deidentified labels to protect patient data in accordance with the procedures outlined in the Institutional Review Board Protocol #10–03832, approved by the UCSF Committee of Human Resources and the Duke University IRB (Pro00054515).

Animals and Animal Care—Animal husbandry and all procedures on mice were carried out in Laboratory Animal Resource Center (LARC) facilities at UCSF Parnassus in accordance with the guidelines stipulated by the Institutional Animal Care Use Committee (IACUC) protocols, #AN133001, #AN179766 and AN194983, which adhere to the NIH Guide for the Care and Use of Laboratory Animals. Mice were maintained in pathogen-free, ventilated HEPA-filtered cages under stable housing conditions of 30–70% humidity, a temperature of 20–26°C, and a 12:12 hour dark:light cycle. All studies involved female mice and littermates were randomly distributed to experimental groups based on genotype. Alternatively, FVB/NJ, C57Bl6/NJ, and NOD/SCID mice were purchased from Jackson Laboratories for orthotopic implantation and limiting dilution transplantation assays. Mice were 6–8 weeks of age for tumor cell orthotopic injections and 3–4 weeks of age for limiting dilution transplantation assays so endogenous mammary epithelium could be cleared. MMTV-PyMT tumor cells were derived from mice on a C57Bl6/NJ background and were implanted into syngeneic mice (6–8 weeks of age) for tumorigenesis assays. LSL-V737N-β1 transgenic mice were generated as described[26] and were maintained on an FVB/NJ or C57Bl6/NJ background. Col1a1^{Tm1Jae} mice were purchased from Jackson laboratories and backcrossed for 10 generations to a clean FVB/NJ background.[67] Mammary tissues were analyzed from female mice at 6 and 10–12 weeks of age. For FACS and qRT-PCR analyses, adult mice were 10–12 weeks old. MMTV-Cre$^{4Mam/J}$, MMTV-PyMT and MMTV-Neu/ErbB2$^{NK1Mul/J}$ mice were purchased from Jackson laboratories on an FVB/NJ background and crossed with LSL-V737N-β1 and Col1a1^{Tm1Jae} mice.[114,115] For lineage tracing, K5-Cre/ERT2 mice were obtained from Dr. Ophir Klein (UCSF) and MMTV-PyMT/R26-Brainbow2.1 mice[116] were obtained from Dr. Mikala Egeblad (Cold Spring Harbor) and maintained on a C57Bl6/NJ background. Note that for analysis of LSL-V737N-β1/ K5-Cre/ERT2 mice (V737N^{K5}), three subsequent daily low doses of tamoxifen were administered during puberty (4–5 weeks of age), to minimize the impact of disruption to estrogen signaling on ductal outgrowth and to reduce any potential targeting of bipotent progenitor MECs.[117] A later time point of analysis was chosen for the V737N^{K5} mice (12 weeks) to allow additional time for homeostatic conditions to establish following tamoxifen treatment, and due to the reported potential for variable ovarian hormone responses on the C57Bl6/NJ mouse strain.[113]

Human breast cancer cell lines—T47D and MCF7 human breast cancer cell lines derived from female patients were sourced from the ATCC (American Type Culture Collection). Cell lines were authenticated by the source (ATCC, confirmed low passage number) as well as immunoblotting for the expression of proteins known to characterize the cell lines, such as Estrogen Receptor alpha and the Progesterone Receptor. All cell lines tested negative for mycoplasma contamination. T47D and MCF7 were cultured as recommended in RPMI with 10% FBS and DMEM with 10% FBS, respectively, and incubated at a temperature of 37°C, 5% carbon dioxide, and 95% humidity. Cells were cultured on polyacrylamide gels of low and high stiffnesses (400 Pa and 6 kPa), serum starved overnight and then treated for 15 min with R5020 (10 nM) and EGF (20 ng/mL) alone or in combination.

METHOD DETAILS

Primary mammary epithelial cell colony formation assays—Primary FACS-isolated mouse luminal and basal MECs were plated at a density of 5000 cells and 1000 cells respectively in ~20 uL of 100% rBM (R&D Systems, Cultrex BME) by pipetting around the edge of the well of a 96 well plate. Cell Medium (DMEM-F12) containing 1% FBS, 500 ng/mL hydrocortisone, 5 μg/mL insulin and 20 ng/mL EGF was added to each well and colonies were counted after 10–14 days in culture with media exchanges every 2–3 days. In some cases, primary colonies were harvested from rBM gels using cell recovery solution (Corning, Cat. #: 354253), dissociated to single cells with Trypsin/EDTA, counted and then plated at the above densities to assess their proficiency at secondary colony formation. Resulting colonies were re-counted after 10–14 days of culture with media exchanges every 2–3 days. For human tissues, fresh FACS isolated luminal and basal MECs were resuspended in rBM at a density of at 50,000 cells/mL, and 20 μL droplets (1000 cells) were seeded into 8-well chamber slides (LabTek II, Cat. #: 154534) and allowed to set at 37 °C. Wells were filled 0.4 mL cell medium (DMEM/F-12) containing Glutamax, B27 Supplement (Gibco, Cat. #: 17504044), 500 ng/mL hydrocortisone, 5 μg/mL insulin, 10 ng/mL EGF and 20 ng/ml Cholera Toxin from *Vibrio cholerae* (Sigma, C8052). Cells were cultured for 7–10 days prior to counting the number of colonies per well.

Collagen/rBM hydrogels for primary mouse MEC culture, hormone and inhibitor treatment—Primary mouse MEC organoids were prepared by manual chopping of mouse mammary gland tissues harvested from 10–12-week-old mice followed by digestion with shaking for 1 hr at 37 °C with Collagenase A from Clostridium histolyticum (10 mg/mL; Roche, Cat. #: 13560925) and Hyaluronidase from bovine testes (1 mg/mL, Sigma-Aldrich, Cat. #: H3506) in DMEM/F12 supplemented with 1% FBS. Digests were then pelleted by centrifugation (1200 rpm), washed in PBS with 2% FBS (Wash buffer) and digested for a further 5 min with Dispase II from *Bacillus polymyxa* (2.5 mg/mL, Sigma-Aldrich, Cat. #: D4693) and DNAse I from bovine pancreas (100 μg/mL; Roche, Cat. #: 10104159001). A final digestion with 0.25% Trypsin-EDTA solution was performed for single cell dissociation. Single cells were cultured in rBM (6%) for 10–14 days prior to their recovery from rBM and resuspension in Col1/rBM hydrogels prepared as described.[25,48,83] Hydrogels were prepared from Rat Tail collagen I (Corning) incubated for >10 days with 0.1% acetic acid containing 500 mM L-Ribose (Chem Impex International) (crosslinked; STIFF) or 0.1% acetic acid alone (non-crosslnked; SOFT). Collagen was then mixed with 20% rBM, DMEM, PBS and 1 μg/mL Human Plasma Fibronectin Purified Protein (Sigma-Aldrich, Cat. #: FC010). 1N NaOH was added to achieve a neutral ~pH and a thin base layer of 100 μL volume was added to the well of a 48-well tissue culture plate precoated with 1% agarose. Mammary organoids were resuspended in the SOFT and STIFF collagen preparations and plated as a top layer of 100 μL and allowed to solidify for 30 min at room temperature followed by 30 min at 37 °C. Cell medium was then added, and gels were detached from the sides of the wells to remain suspended in cell medium. Alternatively, following light trypsinization, organoids were immediately cultured in Col1/rBM hydrogels without preparatory culture in 100% rBM. Organoids were cultured in DMEM/F12 supplemented with 20 ng/mL Epidermal Growth Factor (EGF), 10 μg/mL Insulin and 2 μg/mL hydrocortisone. Organoid/hydrogel cultures were serum

starved overnight before treatment with EGF (20 ng/mL) and promegestone/R5020 (1, 10, 100 nM; Perkin Elmer, Cat. #: NLP00400) and 10 nM R5020 with or without the addition of FAK (1 μM; PND-1186, Chem Scene, Cat. #: 1061353–68-1) and EGFRi (Tyrphostin/ AG-1478, Selleck Chem, Cat. #: S2728) inhibitors (FAKi and EGFRi). TRIZol (Invitrogen) was used for RNA extraction using the Ambion mirVana kit (Invitrogen, Cat. #: AM1560) per manufacturer's instructions.

Lineage tracing in mice—Lineage tracing in mice was performed using R26-Confetti reporter mice, which were bred with LSL-V737N-β1 mice and K5-Cre/ERT2 mice. Lineage tracing and V737N-β1-integrin expression were induced primarily in basal lineage MECs by a single intraperitoneal injection of Tamoxifen (Cayman Chemical, Cat. #: 13258, 1.5 mg) in pubertal mice at 3–4 weeks of age. Lineage tracing was assessed at two time points (2 and 16 weeks) post tamoxifen induction, when mammary glands were excised and fixed with 4% paraformaldehyde for 30 min prior to embedding and freezing in OCT. A cryostat was used to cut 40 μm thick mammary gland sections which were then stained with Alexa Fluor (AF) 647 Phalloidin (Invitrogen, Cat. #: A22287) to visualize actin filaments when analyzing lineage clonality using a Leica TCS SP5 (five channels) Confocal Microscope with Leica Application Suite (LAS) software. Clonality was assessed by counting the number of clones present in uniformly sized segments of mammary ductal epithelium and counting the number of cells constituting each clone.

RANKL inhibition in mice—10-week-old CTL^{M} and $V737N^{M}$ mice and WT and COL mice were treated with control antibody (Mu:Fc) or RANK-Fc^{118} (AMGEN, 10 mg/kg) by intraperitoneal injection 3 times per week for a period of two weeks (6 total injections) prior to mammary gland harvest and MEC isolation for limiting dilution transplantation assays. For premalignant lesion studies, the same treatment regimen was used with initiation at 10 weeks of age in Neu and $V737N^{Neu}$ mice and at 5 weeks of age in PyMT and COL^{PyMT} mice.

ERK inhibition in mice—10-week-old CTL^{M} and $V737N^{M}$ mice were treated orally by gavage with vehicle (hydroxyethylcellulose 1% (w/v)/P80 0.25% (v/v)) or the ERK inhibitor, LY3214996 (Temuterkib, from InvivoChem, Cat. #: V3178, 20 mg/kg) 3 times per week for a period of two weeks (6 total injections) prior to mammary gland harvest and MEC isolation for limiting dilution transplantation assays.[119]

Collagen/rBM hyrdrogels with orthotopic implantation of tumor cells—Rat tail collagen-1 (High concentration, Corning, Cat. #: 354249) was incubated with 0.1% acetic acid (non-crosslinked; SOFT) or 0.1% acetic acid with 500 mM L-ribose (Chem Impex International, Cat. #: 28127) (cross-linked; STIFF) for at least 10 days before preparation of Col1/ rBM hydrogels for orthotopic implantation of tumor cells or tumor fragments.[26,48] Col1 mixtures were then combined with basement membrane extract (R&D Systems, Cultrex BME, type 2, Pathclear, Cat. #: 3532–005-02) (20% final volume), PBS and 1N NaOH to a slightly acidic pH (pH ~6.5) as determined by pH strips. PyMT tumor cells were resuspended in Col1/rBM preparations and maintained at 4 °C until implantation into the inguinal mammary fat pad of syngeneic mice.

Monitoring of Tumor growth and metastasis—Tumor growth was monitored by palpation and caliper measurement weekly or biweekly. For end point studies, mice were sacrificed when tumors reached maximum tumor volume (1.5 cm in diameter). For early and premalignant lesion analysis of mammary tissues, genetically engineered mouse models were sacrificed at specific time points depending on their established rates of tumor progression on the various background mouse strains used (Neu and $V737N^{Neu}$ FVB/NJ mice at 20 weeks of age; PyMT and COL^{PyMT} FVB/NJ mice at 8 weeks of age; PyMT and K5-$V737N^{PyMT}$ C57Bl6/J mice at 12 weeks of age). Lung metastases were quantified by counting of surface lesions at time of animal sacrifice, and by examination of histological lung sections stained by H&E. Tissue sections were scanned using a ZEISS Axio Scan.Z1 digital slide scanner equipped with CMOS and color cameras, 10x, 20x and 40x objectives, and lesion areas were determined by tracing in QuPath.[120]

Quantitative Reverse transcriptase-polymerase chain reaction (qRT-PCR)—RNA was prepared from FACS-isolated MECs or flash frozen and pulverized mammary tumor tissues using TRIZol reagent (Invitrogen). Reverse transcription reactions were performed using M-MLV reverse transcriptase (Biochain, Cat. #: Z5040002) with random hexamer primers. cDNA was mixed with PerfeCTa SYBR Green FastMix (Quantibio, Cat. #: 95072–05K) for qPCR analysis using an Eppendorf realplex2 epgradient S mastercycler. Thermal cycling conditions were 10 min at 95 °C, followed by 40 cycles of 15s at 95 °C and 45 s at 65 °C. Melting curve analysis was used to verify primer pair specificity. Relative mRNA expression was determined by the ΔΔCT method with normalization to *GAPDH*, *18S* or *KRT8*.

Immunohistochemistry (IHC)—IHC was performed as described[90] using antibodies specific to E-cadherin (BD Biosciences, clone 36, Cat. #: 610181, 1:400), ALDH (BD Biosciences, clone 44, Cat. #: 611194, 1:200), p-Histone H3 (Ser 10)-R (Santa Cruz, Cat. #: sc-8656-R, 1:200) and cleaved Caspase-3 (Asp175) (Cell Signaling Technology, Cat. #: 9661S, 1:200). Briefly, antigen retrieval was accomplished by boiling sections in 10 mM citrate buffer (10min). Following primary antibody incubation overnight at 4 °C, sections were incubated for 1 hr with species-specific Horseradish Peroxidase (HRP)-conjugated secondary antibodies (ImmPRESS HRP Goat Anti-Mouse or Rabbit IgG Polymer Detection Kit, Peroxidase, Vector Laboratories, Cat. #: MP-7452 and MP-7451) before developing positive staining with ImmPACT DAB Substrate Peroxidase (HRP, Vector Laboratories, Cat. #: SK-4105). Images of stained sections were acquired with an Olympus microscope (IX81) and 10x, 20x or 40x objectives.

Immunofluorescence—Immunofluorescence was performed using the following specific antibodies: phospho-p130-Cas (Y410) (Cell Signaling Technology, Cat. #: 4011, 1:200), phospho-FAK (Y397) (Cell Signaling Technology, Cat. #: 8556, 1:200), phospho-FAK (Y397) (Thermo Fischer Scientific, clone 141–9, Cat. #: 44–625G), phospho-p44/42 MAPK (ERK1/2) (T202/Y204) (Cell Signaling Technology, Cat. #: 9101, 1:200), NFκB p65 (D14E12) XP (Cell Signaling Technology, Cat. #: 8242), phospho-Histone H3 (S10) (Cell Signaling Technology, Cat. #: 9701, 1:200), cleaved caspase-3 (Asp175) (Cell Signaling Technology, Cat. #: 9661, 1:200), Integrin β1, activated (MilliporeSigma, clone HUTS-4,

Cat. #: MAB2079Z, 1:400), Integrin-β1 (MilliporeSigma, clone JB1A, Cat. #: MAB1965, 1:400), CD29 (BD Biosciences, clone 9EG7, Cat. #: 553715, 1:400), PR (Thermo Fischer Scientific, clone hPRa7, Cat. #: MA5–12658, 1:100), ERα (Abcam, Cat. #: ab37438, 1:200), Alexa Fluor (AF)488 K8 (Abcam, clone EP1628Y, Cat. #: ab192467, 1:200), K14 (Covance, Cat. #: PRB-155P, 1:400), TRANCE/TNFSF11/RANKL (R&D Biosystems, Cat. # AF462, 1:200), RANKL (Amgen, Cat. #: M366), K8+18 (Fitzgerald, Cat. #: 20R-CP004, 1:400), K5 (Fitzgerald, Cat. #: 20R-CP003, 1:400), RANK (Amgen, Cat. #: N1H8, 1:200), RANK (R&D Biosystems, Cat. # AF692, 1:200), SLUG (C19G7) (Cell Signaling Technology, Cat. #: 9585, 1:200), ZEB1 (E2G6Y) (Cell Signaling Technology, Cat. #: 70512, 1:200) and a custom phosphor-specific antibody targeting PR Ser294 (clone 8508; 1:200) that was generously provided by Dr. Carol Lange[79]. Briefly, frozen sections were fixed in 2% paraformaldehyde, prior to permeabilization with 3% triton-x-100 and incubation with primary antibodies overnight at 4 °C. The next morning, sections were incubated with species specific secondary antibodies conjugated to different fluorophores (AF-633, −555, −568, −488, Invitrogen) and CNA-35-GFP (Addgene Plasimd #61603; 1:500) when specified. All washes were carried out using Tris-buffered saline with 0.5% Tween-20 and nuclei and/or actin filaments were counterstained using 4′,6-diamidino-2-phenylindole (DAPI, Cat. #: D1306) or the appropriate Phalloidin-fluorophore conjugate (AF488, AF647, Cat. #'s: A12379 and A22287), respectively. Images of stained sections were acquired either on: an inverted Eclipse Ti-E Nikon microscope with CSU-X1 spinning disk confocal (Yokogawa Electric Corporation), 405 nm, 488 nm, 561, 635 nm lasers; a Plan Apo VC 60X/1.40 Oil or an Apo LWD 40X/1.15 Water-immersion λS objective; electronic shutters; a charge-coupled device (CCD) camera (Clara; Andor) and controlled by Metamorph; a Nikon Ti Microscope (Inverted) with CSU-W1 widefield spinning disk confocal (Andor Borealis), 100 mW at 405, 561, and 640 nm; 150 mW at 488 nm lasers, an Andor Zyla sCMOS camera (5.5 megapixels) and Andor iXon Ultra DU888 1k x 1k Electron multiplying CCD to enable large field of view confocal imaging and controlled by Micromanager; or a Nikon SoRa Spinning Disk microscope controlled by NIS Elements software (version 5.41.02).

Image Analysis—Image analysis of IHC and immunofluorescence was performed using ImageJ and QuPath software.[120,121] For comparison, immunofluorescence images were subjected to same-level thresholding based on a determined range of positive fluorescence intensity for each channel and antibody staining panel. The threshold area (μm) was expressed as percentage of cell type-specific or nuclear area using basal or luminal cytokeratins or DAPI staining, respectively. Specifically, DAPI and/or epithelial cytokeratin staining was used to make a mask over total or nuclear epithelial cell area to then determine the percent positive staining area of the antibody in question. Other IHC analysis was performed using the IHC profiler ImageJ plugin as described.[122] Normal ductal structures, premalignant and early malignant lesions for mouse models were scored by selecting epithelium using the QuPath annotations tool and classifying each annotation as either normal or early lesion.

Fluorescence activated cell sorting (FACS), primary MEC and TIC isolation —Tissues were digested as described above, spun down at 1200 rpm and washed with

FACS wash buffer (PBS with 2% FBS). Cells were then blocked with mouse and rat serum (Jackson Immunoresearch Laboratories, Cat. #: AB_2337194 and AB_2337141) and TruStain FcX antibody (anti-mouse CD16/32) (BioLegend, clone 93, Cat. #: 101319) for 10 min, followed by incubation for 25 min at 4° C with the following mouse specific antibodies to delineate subpopulations: CD24-PE (BD Biosciences, clone M1/69, Cat, #: 553262, 1:100), CD49f -PE-Cy7 (BioLegend, clone GoH3, Cat: #: 313621, 1:100), CD31-APC (BioLegend, clone 390, Cat: #: 102409, 1:40), CD45-APC (BioLegend, clone 30-F11, Cat: #: 103111, 1:160), and TER-119-APC (BioLegend, clone TER-119, Cat: #: 116211, 1:80), CD61-FITC (BioLegend, clone 2C9.G2 (HMβ3–1), Cat. #: 104305, 1:20), and CD61-AF647 (BioLegend, clone 2C9.G2 (HMβ3–1), Cat. #: 104313, 1:100). Human tissues were incubated for 25 min at 4 °C with the following primary antibodies: CD24-PE (BioLegend, clone ML5, Cat, #: 311105, 1:100), CD44-FITC (BioLegend, clone IM7, Cat: #: 103021, 1:20), EPCAM CD326-FITC (Thermo Fischer Scientific, clone VU-1D9, Cat. #: A15755, 1:100), CD49f-PE-Cy7 (BioLegend, clone GoH3, Cat: #: 313621, 1:100), CD31-PE (BioLegend, clone WM59, Cat: #: 303105, 1:40), CD45-PE (BioLegend, clone H130, Cat: #: 304007, 1:100) and CD235-α-PE (BD Biosciences, clone GA-R2, Cat: #: 561051, 1:100). MEC lineage negative populations were removed by positive APC-CD45/CD31/TER-119 (mouse) and PE-CD45/CD31/CD235-α (human) staining. Cells were washed with FACS wash buffer and with DAPI in PBS for 5 min to distinguish live/dead cells. BD FACSAria II cell sorters were used to conduct cell sorting using FACSDiva software (BD Biosceinces). Data was analyzed using FlowJo software (Tree Star). Isolated cells were collected and used for RNA isolation, colony formation assays or limiting dilution transplantation assays as described above.

Mammary gland wholemounts and branching quantification—Inguinal mammary glands wholemounts were allowed to dry for 30 min prior to fixation and staining. For H&E staining, mammary glands were fixed in 4% paraformaldehyde prior to dehydration in xylene/alcohol series, H&E counterstained, and mounted with permount. For Carmine alum staining, glands were fixed with Carnoy's solution (60% ethanol, 30% chloroform and 10% glacial acetic acid) and stained overnight in Carmine alum (0.2% carmine and 0.5% potassium aluminum sulfate in water) prior to dehydration, clearing in xylene and mounting with permount. Primary branches were defined as ducts terminating in an end bud. Secondary and tertiary branches were defined as branches bifurcating from primary ducts or secondary branches, respectively. Terminal end bud and branching analysis was performed using ImageJ. The number of terminal end buds were counted per mammary gland, and their average area (μm^2) measured. Branching was quantified by tracing an average of 5 primary ductal structures and counting the number of secondary and tertiary branches.

Limiting dilution transplantation assays (LDTAs)—LDTAs were performed as described[123] using FACS isolated MECs. Briefly, CD24+CD49f^{hi} MECs (basal/myoepithelial) or PyMT tumor cells were counted such that increasing dilutions could be prepared (1000, 100, 50, 10 cells) for injection into a cleared inguinal mammary fat pad. The inguinal mammary fat pads of 3–4-week-old mice were cleared of their endogenous epithelium by removing the portion of the fat pad proximal to the lymph node. For normal MECs, the basal population was double sorted prior to cell transplantation.

Clearance was verified by mounting resected glands on histology slides, fixing in Carnoy's solution, and staining with Carmine alum. Stem cell frequency was determined at 6 weeks post transplantation by the appearance of progressing tumors (PyMT tumor cells) or by examining mammary glands for epithelial ductal outgrowths as determined upon their harvest for mounting, fixation and carmine aluminum staining as described. Repopulating events were scored as positive outgrowths with evidence of ductal branching. For PyMT tumor LDTAs, three tumors each of the primary LDTAs taken from SOFT and STIFF ECM stroma conditions were pooled before counting cells and repeating the LDTA for secondary tumor formation. Tumor initiating cell and mammary epithelial progenitor cell frequency were determined by counting the number of positive outgrowths (tumor or ductal epithelium) from transplants made at each cell dilution and using an Extreme Limiting Dilution Analysis software application webtool (score test for differences in stem cell frequencies) from The Walter and Eliza Hall Institute of Medical Research (http://bioinf.wehi.edu.au/software/elda/).[124]

Atomic Force Microscopy (AFM)—AFM was performed and analyzed as described[17] using an MFP3D-BIO inverted optical AFM (Asylum Research, Santa Barbara, CA) mounted on a Nikon TE200-U inverted microscope (Melville, NY) and placed on a vibration-isolation table (Herzan TS-150). Briefly, tissue specimens (20 μm thickness) were allowed to thaw and equilibrate to room temperature before immersion in PBS supplemented with 1 ug/mL propidium iodide, and protease and phosphatase inhibitor cocktail solutions (genDEPOT, Xpert solutions, Cat. #: P3100 and P3200). Silicon nitride cantilevers were used with a nominal spring constant of 0.06 N m^{-1} and a borosilicate glass spherical tip with 5 μm diameter (Novascan Technologies). Cantilevers were calibrated using the thermal fluctuation method. AFM force maps were performed on 40 × 40 μm fields from two different quadrants of the same non-malignant human breast specimen. Elastic moduli measurements were derived from force curves obtained utilizing the FMAP function of the Igor Pro v. 6.22A (WaveMetrics, Lake Oswego, OR) supplied by Asylum Research. Cells were assumed to be incompressible and a Poisson's ratio of 0.5 was used in the calculation of the Young's elastic modulus. AFM measurements were generated for up to one hour after thawing tissues. Periductal stromal ECM-rich regions were selected to generate all force maps and single point indentations for each patient specimen.

Picrosirius red staining—FFPE tissues were dewaxed and rehydrated, and were then stained with 0.1% picrosirius red (Direct Red 80, Sigma-Aldrich, 365,548 and picric acid solution, Sigma-Aldrich, P6744) for 1 hr and counterstained with Weigert's hematoxylin (Thermo Scientific, 88028 and 88029) for 10 min at RT. Polarized light images were acquired using an Olympus IX81 microscope fitted with an analyser (U-ANT) and a polarizer (U-POT, Olympus) oriented parallel and orthogonal to each other.

Vaginal cytology for estrus cycle determination—The estrus cycle in mice was determined by vaginal cytology as described[72]. Briefly, a thin cotton tipped applicator (Puritan, Cat. #: 25–826 5WC) was immersed in sterile PBS prior to insertion into the vaginal cavity to collect fluid. The cotton tipped applicator was then smeared onto the well of a 24-well tissue culture plate before staining cells with crystal violet solution

(0.2%). Wells were then examined under brightfield with an Olympus microscope (IX81) to determine the stage of estrus (proestrus, diestrus, metestrus and estrus) for each mouse by the cell content and morphology present.

Enzyme-linked immunosorbent assay (ELISA)—ELISAs were performed using Mouse TRANCE/RANKL/TNFSF11 DuoSet ELISA Kits (R&D Biosystems, Cat. #: DY462) according to the manufacturer's directions.

Mammography—All mammography was conducted by licensed physicians at the UCSF and Duke medical centers according to established protocols as described.[48,125] Quantitative measurements of the raw mammography images used the automated volumetric density measure developed by Dr. John Shepherd.[126]

Cell fractionation, Immunoblotting and Densitometry—When indicated, cell lysates from FACS isolated MECs, whole mammary gland or mammary tumor tissues were prepared to fractionate nuclear and cytoplasmic cellular compartments using Thermo Scientific NE-PER Nuclear and Cytoplasmic Extraction Reagents (Cat. #: 78833). Other cell lysates were prepared using RIPA buffer (150 mM NaCl, 1% NP40, 0.5% sodium deoxycholate, 0.1% sodium dodecyl sulphate, 50 mM Tris-HCl, pH 8.0) and all lysates were supplemented with protease and phosphatase inhibitor cocktail solutions (genDEPOT, Xpert solutions, Cat. #: P3100 and P3200). Immunoblotting was performed as described[127] using Immobilon P Polyvinylidene difluoride membrane (PVDF, Millipore, Cat. #: IPVH00010) for protein transfer, and incubation with the following primary antibodies: phospho-p44/42 MAPK (ERK1/2) (T202/Y204) (Cell Signaling Technology, Cat. #: 9101, 1:1000), p44/42 MAPK (ERK1/2) (Cell Signaling Technology, Cat. #: 9102, 1:1000), phospho-PR (S294) (Thermo Fischer Scientific, Cat. #: PA5–37472, 1:200), phospho-PR (S294) (Thermo Fischer Scientific, Cat. #: MA1–414, 1:200), PR (Santa Cruz Biotechnology, clone H-190, Cat. #: sc-7208, 1:500), PR (Thermo Fischer Scientific, clone hPRa7, Cat. #: MA5–12658, 1:500), NFκB-p65 (D14E12) XP (Cell Signaling Technology, Cat. #: 8242, 1:1000), FAK (D2R2E) (Cell Signaling Technology, Cat. #: 13009P, 1:1000) and Lamin B1 (Abcam, Cat. #: ab16048, 1:2000). Immunoblots were then incubated with the appropriate species specific HRP-conjugated secondary antibodies (Advansta) before developing reactivity with pierce enhanced chemiluminescence (ECL) reagent (Advansta WesternBright ECL HRP substrate, Cat. #: K-12045). Membrane signals were visualized with a PXi imaging system (Syngene). Densitometry measurements were made using ImageJ software with normalization to background membrane density and sample processing control protein levels. Lamin B1 was used for normalization of nuclear extracts (Figure 5C and Figure S4H) and phosphoprotein levels were normalized to their corresponding total protein levels.

Polyacrylamide hydrogels—Polyacrylamide hydrogels of varying rigidities were prepared as described.[128,129] Briefly, compliant Polyacrylamide hydrogels were polymerized on silanized coverslips and functionalized with Fibronectin (1μg/mL) overnight. PA gels were washed three times and equilibrated overnight with cell media at 37 °C prior to cell seeding. Cells were cultured for 24 hr on hydrogels prior to treatment and cell lysis for immunoblotting.

STIFMap image generation—STIFMap images were generated as previously described.[55] Briefly, immunostained images were resized to the same resolution, and decomposed into squares of the same dimensions, as the panels used to train the neural networks. The elasticity of each image was then predicted using five independently trained models with different brightness, sharpness, and contrast transformations. STIFMaps are depicted as collagen pseudocolored to reflect the predicted elasticity, and overlayed with EMT marker staining. This analysis was performed using code available at https://github.com/cstashko/STIFMaps.

QUANTIFICATION AND STATISTICAL ANALYSIS

GraphPad Prism Version 10.0.2 was used to perform all statistical analyses and correlations and statistical significance was determined using the appropriate tests as noted in the corresponding figure legends. Tests of normality that incorporated skewness and kurtosis were used to determine the appropriate statistical test.[130] All independent variables are described in the figure legends with measurements always from distinct samples (biological replicates) unless otherwise stated. All tests are two-tailed unless otherwise indicated. For all analyses, samples were randomized. Patient and mouse samples were monitored by unique identifiers and mouse littermates were evenly distributed across different experimental groups to avoid any potential bias. Sample sizes were mouse studies were based on published work where statistical differences were found between transformed mammary cells admixed with control fibroblasts or lysyl-oxidase overexpressing fibroblasts transplanted into the mammary fat pad of mice, as well as MMTV-Neu or MMTV-PyMT mice treated with b-aminopropionitrile (BAPN), an inhibitor of LOX activity.[25,26] Evaluations for clinical studies were determined based on statistical differences in ECM stiffness measurements among human patients determined by AFM in previously published work,[17,48] as well as sample availability.

Supplementary Material

Refer to Web version on PubMed Central for supplementary material.

ACKNOWLEDGEMENTS

We thank Lydia and Nataliya Korets for technical support and Susan Samson for patient advocacy, and support from the Nikon Imaging Center and Biological Imaging Development Center and the Parnassus Flow Cytometry Core. Work was supported by these grants: NIH shared equipment S10OD028611-01; US National Institutes of Health/National Cancer Institute 1R01CA222508-01, R01CA192914 and 1R35CA242447-01A1, US Department of Defense (DOD) Breast Cancer Research Program BC122990, Give Breast Cancer the Boot pilot project, and BCRF A132292 (V.M.W.); and American Association for Cancer Research 15-40-01-NORT: Basic Cancer Research Fellowship, and 17-40-48-NORT: AACR Janssen Cancer Interception Research Fellowship (J.J.N.).

REFERENCES

1. Tomasetti C, Li L, and Vogelstein B. (2017). Stem cell divisions, somatic mutations, cancer etiology, and cancer prevention. Science 355, 1330–1334. 10.1126/science.aaf9011. [PubMed: 28336671]
2. Tomasetti C, and Vogelstein B. (2015). Cancer etiology. Variation in cancer risk among tissues can be explained by the number of stem cell divisions. Science 347, 78–81. 10.1126/science.1260825. [PubMed: 25554788]

3. Blokzijl F, de Ligt J, Jager M, Sasselli V, Roerink S, Sasaki N, Huch M, Boymans S, Kuijk E, Prins P, et al. (2016). Tissue-specific mutation accumulation in human adult stem cells during life. Nature 538, 260–264. 10.1038/nature19768. [PubMed: 27698416]

4. Shibue T, and Weinberg RA (2017). EMT, CSCs, and drug resistance: the mechanistic link and clinical implications. Nat Rev Clin Oncol 14, 611–629. 10.1038/nrclinonc.2017.44. [PubMed: 28397828]

5. Taube JH, Herschkowitz JI, Komurov K, Zhou AY, Gupta S, Yang J, Hartwell K, Onder TT, Gupta PB, Evans KW, et al. (2010). Core epithelial-to-mesenchymal transition interactome gene-expression signature is associated with claudin-low and metaplastic breast cancer subtypes. Proc Natl Acad Sci U S A 107, 15449–15454. 10.1073/pnas.1004900107. [PubMed: 20713713]

6. Prat A, Parker JS, Karginova O, Fan C, Livasy C, Herschkowitz JI, He X, and Perou CM (2010). Phenotypic and molecular characterization of the claudin-low intrinsic subtype of breast cancer. Breast Cancer Res 12, R68. 10.1186/bcr2635. [PubMed: 20813035]

7. Glinsky GV (2008). “Stemness” genomics law governs clinical behavior of human cancer: implications for decision making in disease management. J Clin Oncol 26, 2846–2853. [PubMed: 18539963]

8. Bierie B, Pierce SE, Kroeger C, Stover DG, Pattabiraman DR, Thiru P, Liu Donaher J, Reinhardt F, Chaffer CL, Keckesova Z, and Weinberg RA (2017). Integrin-beta4 identifies cancer stem cell-enriched populations of partially mesenchymal carcinoma cells. Proc Natl Acad Sci U S A 114, E2337–E2346. 10.1073/pnas.1618298114. [PubMed: 28270621]

9. Northey JJ, Przybyla L, and Weaver VM (2017). Tissue Force Programs Cell Fate and Tumor Aggression. Cancer Discov 7, 1224–1237. 10.1158/2159-8290.CD-16-0733. [PubMed: 29038232]

10. Visvader JE (2011). Cells of origin in cancer. Nature 469, 314–322. 10.1038/nature09781. [PubMed: 21248838]

11. Hayward MK, Muncie JM, and Weaver VM (2021). Tissue mechanics in stem cell fate, development, and cancer. Dev Cell. 10.1016/j.devcel.2021.05.011.

12. Engler AJ, Sen S, Sweeney HL, and Discher DE (2006). Matrix elasticity directs stem cell lineage specification. Cell 126, 677–689. [PubMed: 16923388]

13. Engler AJ, Griffin MA, Sen S, Bonnemann CG, Sweeney HL, and Discher DE (2004). Myotubes differentiate optimally on substrates with tissue-like stiffness: pathological implications for soft or stiff microenvironments. J Cell Biol 166, 877–887. 10.1083/jcb.200405004.jcb.200405004 [pii]. [PubMed: 15364962]

14. Przybyla L, Lakins JN, and Weaver VM (2016). Tissue Mechanics Orchestrate Wnt-Dependent Human Embryonic Stem Cell Differentiation. Cell Stem Cell 19, 462–475. 10.1016/j.stem.2016.06.018. [PubMed: 27452175]

15. Muncie JM, Ayad NME, Lakins JN, Xue X, Fu J, and Weaver VM (2020). Mechanical Tension Promotes Formation of Gastrulation-like Nodes and Patterns Mesoderm Specification in Human Embryonic Stem Cells. Dev Cell 55, 679–694 e611. 10.1016/j.devcel.2020.10.015. [PubMed: 33207224]

16. Maller O, Drain AP, Barrett AS, Borgquist S, Ruffell B, Zakharevich I, Pham TT, Gruosso T, Kuasne H, Lakins JN, et al. (2021). Tumour-associated macrophages drive stromal cell-dependent collagen crosslinking and stiffening to promote breast cancer aggression. Nat Mater 20, 548–559. 10.1038/s41563-020-00849-5. [PubMed: 33257795]

17. Acerbi I, Cassereau L, Dean I, Shi Q, Au A, Park C, Chen YY, Liphardt J, Hwang ES, and Weaver VM (2015). Human breast cancer invasion and aggression correlates with ECM stiffening and immune cell infiltration. Integr Biol (Camb) 7, 1120–1134. 10.1039/c5ib00040h. [PubMed: 25959051]

18. Pickup MW, Laklai H, Acerbi I, Owens P, Gorska AE, Chytil A, Aakre M, Weaver VM, and Moses HL (2013). Stromally derived lysyl oxidase promotes metastasis of transforming growth factor-beta-deficient mouse mammary carcinomas. Cancer Res 73, 5336–5346. 10.1158/0008-5472.CAN-13-0012. [PubMed: 23856251]

19. Laklai H, Miroshnikova YA, Pickup MW, Collisson EA, Kim GE, Barrett AS, Hill RC, Lakins JN, Schlaepfer DD, Mouw JK, et al. (2016). Genotype tunes pancreatic ductal adenocarcinoma tissue

tension to induce matricellular fibrosis and tumor progression. Nat Med 22, 497–505. 10.1038/nm.4082. [PubMed: 27089513]

20. Guo W, Keckesova Z, Donaher JL, Shibue T, Tischler V, Reinhardt F, Itzkovitz S, Noske A, Zurrer-Hardi U, Bell G, et al. (2012). Slug and Sox9 cooperatively determine the mammary stem cell state. Cell 148, 1015–1028. 10.1016/j.cell.2012.02.008. [PubMed: 22385965]
21. Lambert AW, and Weinberg RA (2021). Linking EMT programmes to normal and neoplastic epithelial stem cells. Nat Rev Cancer 21, 325–338. 10.1038/s41568-021-00332-6. [PubMed: 33547455]
22. Wilson MM, Weinberg RA, Lees JA, and Guen VJ (2020). Emerging Mechanisms by which EMT Programs Control Stemness. Trends Cancer 6, 775–780. 10.1016/j.trecan.2020.03.011. [PubMed: 32312682]
23. Lopez JI, Mouw JK, and Weaver VM (2008). Biomechanical regulation of cell orientation and fate. Oncogene 27, 6981–6993. 10.1038/onc.2008.348. [PubMed: 19029939]
24. Paszek MJ, Zahir N, Johnson KR, Lakins JN, Rozenberg GI, Gefen A, Reinhart-King CA, Margulies SS, Dembo M, Boettiger D, et al. (2005). Tensional homeostasis and the malignant phenotype. Cancer Cell 8, 241–254. 10.1016/j.ccr.2005.08.010. [PubMed: 16169468]
25. Levental KR, Yu H, Kass L, Lakins JN, Egeblad M, Erler JT, Fong SF, Csiszar K, Giaccia A, Weninger W, et al. (2009). Matrix crosslinking forces tumor progression by enhancing integrin signaling. Cell 139, 891–906. 10.1016/j.cell.2009.10.027. [PubMed: 19931152]
26. Mouw JK, Yui Y, Damiano L, Bainer RO, Lakins JN, Acerbi I, Ou G, Wijekoon AC, Levental KR, Gilbert PM, et al. (2014). Tissue mechanics modulate microRNA-dependent PTEN expression to regulate malignant progression. Nat Med 20, 360–367. 10.1038/nm.3497. [PubMed: 24633304]
27. Miroshnikova YA, Mouw JK, Barnes JM, Pickup MW, Lakins JN, Kim Y, Lobo K, Persson AI, Reis GF, McKnight TR, et al. (2016). Tissue mechanics promote IDH1-dependent HIF1alpha-tenascin C feedback to regulate glioblastoma aggression. Nat Cell Biol 18, 1336–1345. 10.1038/ncb3429. [PubMed: 27820599]
28. Rubashkin MG, Cassereau L, Bainer R, DuFort CC, Yui Y, Ou G, Paszek MJ, Davidson MW, Chen YY, and Weaver VM (2014). Force engages vinculin and promotes tumor progression by enhancing PI3K activation of phosphatidylinositol (3,4,5)-triphosphate. Cancer Res 74, 4597–4611. 10.1158/0008-5472.CAN-13-3698. [PubMed: 25183785]
29. Desai SS, Tung JC, Zhou VX, Grenert JP, Malato Y, Rezvani M, Espanol-Suner R, Willenbring H, Weaver VM, and Chang TT (2016). Physiological ranges of matrix rigidity modulate primary mouse hepatocyte function in part through hepatocyte nuclear factor 4 alpha. Hepatology 64, 261–275. 10.1002/hep.28450. [PubMed: 26755329]
30. Han S, Pang MF, and Nelson CM (2018). Substratum stiffness tunes proliferation downstream of Wnt3a in part by regulating integrin-linked kinase and frizzled-1. J Cell Sci 131. 10.1242/jcs.210476.
31. Storch U, Mederos y Schnitzler M, and Gudermann T. (2012). G protein-mediated stretch reception. Am J Physiol Heart Circ Physiol 302, H1241–1249. 10.1152/ajpheart.00818.2011. [PubMed: 22227128]
32. Samuel MS, Lopez JI, McGhee EJ, Croft DR, Strachan D, Timpson P, Munro J, Schroder E, Zhou J, Brunton VG, et al. (2011). Actomyosin-mediated cellular tension drives increased tissue stiffness and beta-catenin activation to induce epidermal hyperplasia and tumor growth. Cancer Cell 19, 776–791. 10.1016/j.ccr.2011.05.008. [PubMed: 21665151]
33. Joshi PA, Jackson HW, Beristain AG, Di Grappa MA, Mote PA, Clarke CL, Stingl J, Waterhouse PD, and Khokha R. (2010). Progesterone induces adult mammary stem cell expansion. Nature 465, 803–807. 10.1038/nature09091. [PubMed: 20445538]
34. Asselin-Labat ML, Vaillant F, Sheridan JM, Pal B, Wu D, Simpson ER, Yasuda H, Smyth GK, Martin TJ, Lindeman GJ, and Visvader JE (2010). Control of mammary stem cell function by steroid hormone signalling. Nature 465, 798–802. 10.1038/nature09027. [PubMed: 20383121]
35. Tanos T, Sflomos G, Echeverria PC, Ayyanan A, Gutierrez M, Delaloye JF, Raffoul W, Fiche M, Dougall W, Schneider P, et al. (2013). Progesterone/RANKL is a major regulatory axis in the human breast. Sci Transl Med 5, 182ra155. 10.1126/scitranslmed.3005654.

36. Yaghjyan L, Colditz GA, Rosner B, and Tamimi RM (2012). Mammographic breast density and breast cancer risk by menopausal status, postmenopausal hormone use and a family history of breast cancer. Cancer Causes Control 23, 785–790. 10.1007/s10552-012-9936-7. [PubMed: 22438073]

37. Harvey JA, Santen RJ, Petroni GR, Bovbjerg VE, Smolkin ME, Sheriff FS, and Russo J. (2008). Histologic changes in the breast with menopausal hormone therapy use: correlation with breast density, estrogen receptor, progesterone receptor, and proliferation indices. Menopause 15, 67–73. 10.1097/gme.0b013e318054e29a. [PubMed: 17558338]

38. Wood CE, Branstetter D, Jacob AP, Cline JM, Register TC, Rohrbach K, Huang LY, Borgerink H, and Dougall WC (2013). Progestin effects on cell proliferation pathways in the postmenopausal mammary gland. Breast Cancer Res 15, R62. 10.1186/bcr3456. [PubMed: 23938070]

39. Boyd NF, Martin LJ, Li Q, Sun L, Chiarelli AM, Hislop G, Yaffe MJ, and Minkin S. (2006). Mammographic density as a surrogate marker for the effects of hormone therapy on risk of breast cancer. Cancer Epidemiol Biomarkers Prev 15, 961–966. 15/5/961 [pii] 10.1158/1055-9965.EPI-05-0762. [PubMed: 16702377]

40. Byrne C, Ursin G, Martin CF, Peck JD, Cole EB, Zeng D, Kim E, Yaffe MD, Boyd NF, Heiss G, et al. (2017). Mammographic Density Change With Estrogen and Progestin Therapy and Breast Cancer Risk. J Natl Cancer Inst 109. 10.1093/jnci/djx001.

41. Mulac-Jericevic B, Lydon JP, DeMayo FJ, and Conneely OM (2003). Defective mammary gland morphogenesis in mice lacking the progesterone receptor B isoform. Proc Natl Acad Sci U S A 100, 9744–9749. 10.1073/pnas.1732707100. [PubMed: 12897242]

42. Aldaz CM, Liao QY, LaBate M, and Johnston DA (1996). Medroxyprogesterone acetate accelerates the development and increases the incidence of mouse mammary tumors induced by dimethylbenzanthracene. Carcinogenesis 17, 2069–2072. [PubMed: 8824536]

43. Joshi PA, Goodwin PJ, and Khokha R. (2015). Progesterone Exposure and Breast Cancer Risk: Understanding the Biological Roots. JAMA Oncol 1, 283–285. 10.1001/jamaoncol.2015.0512. [PubMed: 26181171]

44. Sampayo R, Recouvreux S, and Simian M. (2013). The hyperplastic phenotype in PR-A and PR-B transgenic mice: lessons on the role of estrogen and progesterone receptors in the mouse mammary gland and breast cancer. Vitam Horm 93, 185–201. 10.1016/B978-0-12-416673-8.00012-5. [PubMed: 23810007]

45. Sprague BL, Trentham-Dietz A, Hedman CJ, Wang J, Hemming JD, Hampton JM, Buist DS, Aiello Bowles EJ, Sisney GS, and Burnside ES (2013). Circulating serum xenoestrogens and mammographic breast density. Breast Cancer Res 15, R45. 10.1186/bcr3432. [PubMed: 23710608]

46. Boyd NF, Martin LJ, Yaffe MJ, and Minkin S. (2006). Mammographic density: a hormonally responsive risk factor for breast cancer. J Br Menopause Soc 12, 186–193. 10.1258/136218006779160436. [PubMed: 17178021]

47. Brisson J, Brisson B, Cote G, Maunsell E, Berube S, and Robert J. (2000). Tamoxifen and mammographic breast densities. Cancer Epidemiol Biomarkers Prev 9, 911–915. [PubMed: 11008908]

48. Northey JJ, Barrett AS, Acerbi I, Hayward MK, Talamantes S, Dean IS, Mouw JK, Ponik SM, Lakins JN, Huang PJ, et al. (2020). Stiff stroma increases breast cancer risk by inducing the oncogene ZNF217. J Clin Invest 130, 5721–5737. 10.1172/JCI129249. [PubMed: 32721948]

49. McConnell JC, O'Connell OV, Brennan K, Weiping L, Howe M, Joseph L, Knight D, O'Cualain R, Lim Y, Leek A, et al. (2016). Increased peri-ductal collagen micro-organization may contribute to raised mammographic density. Breast Cancer Res 18, 5. 10.1186/s13058-015-0664-2. [PubMed: 26747277]

50. Duffy SW, Morrish OWE, Allgood PC, Black R, Gillan MGC, Willsher P, Cooke J, Duncan KA, Michell MJ, Dobson HM, et al. (2018). Mammographic density and breast cancer risk in breast screening assessment cases and women with a family history of breast cancer. Eur J Cancer 88, 48–56. 10.1016/j.ejca.2017.10.022. [PubMed: 29190506]

51. Lindstrom S, Thompson DJ, Paterson AD, Li J, Gierach GL, Scott C, Stone J, Douglas JA, dos-Santos-Silva I, Fernandez-Navarro P, et al. (2014). Genome-wide association study identifies

multiple loci associated with both mammographic density and breast cancer risk. Nat Commun 5, 5303. 10.1038/ncomms6303. [PubMed: 25342443]

52. Boyd NF, Martin LJ, Rommens JM, Paterson AD, Minkin S, Yaffe MJ, Stone J, and Hopper JL (2009). Mammographic density: a heritable risk factor for breast cancer. Methods Mol Biol 472, 343–360. 10.1007/978-1-60327-492-0_15. [PubMed: 19107441]
53. Guen VJ, Chavarria TE, Kroger C, Ye X, Weinberg RA, and Lees JA (2017). EMT programs promote basal mammary stem cell and tumor-initiating cell stemness by inducing primary ciliogenesis and Hedgehog signaling. Proc Natl Acad Sci U S A 114, E10532–E10539. 10.1073/pnas.1711534114. [PubMed: 29158396]
54. Mani SA, Guo W, Liao MJ, Eaton EN, Ayyanan A, Zhou AY, Brooks M, Reinhard F, Zhang CC, Shipitsin M, et al. (2008). The epithelial-mesenchymal transition generates cells with properties of stem cells. Cell 133, 704–715. 10.1016/j.cell.2008.03.027. [PubMed: 18485877]
55. Stashko C, Hayward MK, Northey JJ, Pearson N, Ironside AJ, Lakins JN, Oria R, Goyette MA, Mayo L, Russnes HG, et al. (2023). A convolutional neural network STIFMap reveals associations between stromal stiffness and EMT in breast cancer. Nat Commun 14, 3561. 10.1038/s41467-023-39085-1. [PubMed: 37322009]
56. Nguyen QH, Pervolarakis N, Blake K, Ma D, Davis RT, James N, Phung AT, Willey E, Kumar R, Jabart E, et al. (2018). Profiling human breast epithelial cells using single cell RNA sequencing identifies cell diversity. Nat Commun 9, 2028. 10.1038/s41467-018-04334-1. [PubMed: 29795293]
57. Drain AP, Zahir N, Northey JJ, Zhang H, Huang PJ, Maller O, Lakins JN, Yu X, Leight JL, Alston-Mills BP, et al. (2021). Matrix compliance permits NF-kappaB activation to drive therapy resistance in breast cancer. J Exp Med 218. 10.1084/jem.20191360.
58. Maller O, Hansen KC, Lyons TR, Acerbi I, Weaver VM, Prekeris R, Tan AC, and Schedin P. (2013). Collagen architecture in pregnancy-induced protection from breast cancer. J Cell Sci 126, 4108–4110. 10.1242/jcs.121590. [PubMed: 23843613]
59. Ballard MS, Zhu A, Iwai N, Stensrud M, Mapps A, Postiglione MP, Knoblich JA, and Hinck L. (2015). Mammary Stem Cell Self-Renewal Is Regulated by Slit2/Robo1 Signaling through SNAI1 and mINSC. Cell Rep 13, 290–301. 10.1016/j.celrep.2015.09.006. [PubMed: 26440891]
60. Han Y, Villarreal-Ponce A, Gutierrez G Jr., Nguyen Q, Sun P, Wu T, Sui B, Berx G, Brabletz T, Kessenbrock K, et al. (2022). Coordinate control of basal epithelial cell fate and stem cell maintenance by core EMT transcription factor Zeb1. Cell Rep 38, 110240. 10.1016/j.celrep.2021.110240.
61. Soady KJ, Kendrick H, Gao Q, Tutt A, Zvelebil M, Ordonez LD, Quist J, Tan DW, Isacke CM, Grigoriadis A, and Smalley MJ (2015). Mouse mammary stem cells express prognostic markers for triple-negative breast cancer. Breast Cancer Res 17, 31. 10.1186/s13058-015-0539-6. [PubMed: 25849541]
62. Wang D, Cai C, Dong X, Yu QC, Zhang XO, Yang L, and Zeng YA (2015). Identification of multipotent mammary stem cells by protein C receptor expression. Nature 517, 81–84. 10.1038/nature13851. [PubMed: 25327250]
63. Twigger AJ, Engelbrecht LK, Bach K, Schultz-Pernice I, Pensa S, Stenning J, Petricca S, Scheel CH, and Khaled WT (2022). Transcriptional changes in the mammary gland during lactation revealed by single cell sequencing of cells from human milk. Nat Commun 13, 562. 10.1038/s41467-021-27895-0. [PubMed: 35091553]
64. Bach K, Pensa S, Grzelak M, Hadfield J, Adams DJ, Marioni JC, and Khaled WT (2017). Differentiation dynamics of mammary epithelial cells revealed by single-cell RNA sequencing. Nat Commun 8, 2128. 10.1038/s41467-017-02001-5. [PubMed: 29225342]
65. Gray GK, Li CM, Rosenbluth JM, Selfors LM, Girnius N, Lin JR, Schackmann RCJ, Goh WL, Moore K, Shapiro HK, et al. (2022). A human breast atlas integrating single-cell proteomics and transcriptomics. Dev Cell 57, 1400–1420 e1407. 10.1016/j.devcel.2022.05.003. [PubMed: 35617956]
66. Provenzano PP, Inman DR, Eliceiri KW, Knittel JG, Yan L, Rueden CT, White JG, and Keely PJ (2008). Collagen density promotes mammary tumor initiation and progression. BMC Med 6, 11. 10.1186/1741-7015-6-11. [PubMed: 18442412]

67. Liu X, Wu H, Byrne M, Jeffrey J, Krane S, and Jaenisch R. (1995). A targeted mutation at the known collagenase cleavage site in mouse type I collagen impairs tissue remodeling. J Cell Biol 130, 227–237. 10.1083/jcb.130.1.227. [PubMed: 7790374]
68. Barcus CE, O'Leary KA, Brockman JL, Rugowski DE, Liu Y, Garcia N, Yu M, Keely PJ, Eliceiri KW, and Schuler LA (2017). Elevated collagen-I augments tumor progressive signals, intravasation and metastasis of prolactin-induced estrogen receptor alpha positive mammary tumor cells. Breast Cancer Res 19, 9. 10.1186/s13058-017-0801-1. [PubMed: 28103936]
69. Nong Z, O'Neil C, Lei M, Gros R, Watson A, Rizkalla A, Mequanint K, Li S, Frontini MJ, Feng Q, and Pickering JG (2011). Type I collagen cleavage is essential for effective fibrotic repair after myocardial infarction. Am J Pathol 179, 2189–2198. 10.1016/j.ajpath.2011.07.017. [PubMed: 21907695]
70. Skibinski A, Breindel JL, Prat A, Galvan P, Smith E, Rolfs A, Gupta PB, LaBaer J, and Kuperwasser C. (2014). The Hippo transducer TAZ interacts with the SWI/SNF complex to regulate breast epithelial lineage commitment. Cell Rep 6, 1059–1072. 10.1016/j.celrep.2014.02.038. [PubMed: 24613358]
71. van de Moosdijk AA, Fu NY, Rios AC, Visvader JE, and van Amerongen R. (2017). Lineage Tracing of Mammary Stem and Progenitor Cells. Methods Mol Biol 1501, 291–308. 10.1007/978-1-4939-6475-8_15. [PubMed: 27796960]
72. Byers SL, Wiles MV, Dunn SL, and Taft RA (2012). Mouse estrous cycle identification tool and images. PLoS One 7, e35538. 10.1371/journal.pone.0035538. [PubMed: 22514749]
73. Moumen M, Chiche A, Decraene C, Petit V, Gandarillas A, Deugnier MA, Glukhova MA, and Faraldo MM (2013). Myc is required for beta-catenin-mediated mammary stem cell amplification and tumorigenesis. Mol Cancer 12, 132. 10.1186/1476-4598-12-132. [PubMed: 24171719]
74. Rajaram RD, Buric D, Caikovski M, Ayyanan A, Rougemont J, Shan J, Vainio SJ, Yalcin-Ozuysal O, and Brisken C. (2015). Progesterone and Wnt4 control mammary stem cells via myoepithelial crosstalk. EMBO J 34, 641–652. 10.15252/embj.201490434. [PubMed: 25603931]
75. Joshi PA, Waterhouse PD, Kannan N, Narala S, Fang H, Di Grappa MA, Jackson HW, Penninger JM, Eaves C, and Khokha R. (2015). RANK Signaling Amplifies WNT-Responsive Mammary Progenitors through R-SPONDIN1. Stem Cell Reports 5, 31–44. 10.1016/j.stemcr.2015.05.012. [PubMed: 26095608]
76. Dwyer AR, Truong TH, Ostrander JH, and Lange CA (2020). 90 YEARS OF PROGESTERONE: Steroid receptors as MAPK signaling sensors in breast cancer: let the fates decide. J Mol Endocrinol 65, T35–T48. 10.1530/JME-19-0274. [PubMed: 32209723]
77. Truong TH, Dwyer AR, Diep CH, Hu H, Hagen KM, and Lange CA (2019). Phosphorylated Progesterone Receptor Isoforms Mediate Opposing Stem Cell and Proliferative Breast Cancer Cell Fates. Endocrinology 160, 430–446. 10.1210/en.2018-00990. [PubMed: 30597041]
78. Knutson TP, Daniel AR, Fan D, Silverstein KA, Covington KR, Fuqua SA, and Lange CA (2012). Phosphorylated and sumoylation-deficient progesterone receptors drive proliferative gene signatures during breast cancer progression. Breast Cancer Res 14, R95. 10.1186/bcr3211. [PubMed: 22697792]
79. Knutson TP, Truong TH, Ma S, Brady NJ, Sullivan ME, Raj G, Schwertfeger KL, and Lange CA (2017). Posttranslationally modified progesterone receptors direct ligand-specific expression of breast cancer stem cell-associated gene programs. J Hematol Oncol 10, 89. 10.1186/s13045-017-0462-7. [PubMed: 28412963]
80. Lange CA, Shen T, and Horwitz KB (2000). Phosphorylation of human progesterone receptors at serine-294 by mitogen-activated protein kinase signals their degradation by the 26S proteasome. Proc Natl Acad Sci U S A 97, 1032–1037. 10.1073/pnas.97.3.1032. [PubMed: 10655479]
81. Provenzano PP, Inman DR, Eliceiri KW, and Keely PJ (2009). Matrix density-induced mechanoregulation of breast cell phenotype, signaling and gene expression through a FAK-ERK linkage. Oncogene 28, 4326–4343. 10.1038/onc.2009.299. [PubMed: 19826415]
82. Lopez JI, Kang I, You WK, McDonald DM, and Weaver VM (2011). In situ force mapping of mammary gland transformation. Integr Biol (Camb) 3, 910–921. 10.1039/c1ib00043h. [PubMed: 21842067]

83. Girton TS, Oegema TR, and Tranquillo RT (1999). Exploiting glycation to stiffen and strengthen tissue equivalents for tissue engineering. J Biomed Mater Res 46, 87–92. 10.1002/(sici)1097-4636(199907)46:1<87::aid-jbm10>3.0.co;2-k. [PubMed: 10357139]
84. Lin EY, Jones JG, Li P, Zhu L, Whitney KD, Muller WJ, and Pollard JW (2003). Progression to malignancy in the polyoma middle T oncoprotein mouse breast cancer model provides a reliable model for human diseases. Am J Pathol 163, 2113–2126. 10.1016/S0002-9440(10)63568-7. [PubMed: 14578209]
85. Attalla S, Taifour T, Bui T, and Muller W. (2021). Insights from transgenic mouse models of PyMT-induced breast cancer: recapitulating human breast cancer progression in vivo. Oncogene 40, 475–491. 10.1038/s41388-020-01560-0. [PubMed: 33235291]
86. Gonzalez-Suarez E, Jacob AP, Jones J, Miller R, Roudier-Meyer MP, Erwert R, Pinkas J, Branstetter D, and Dougall WC (2010). RANK ligand mediates progestin-induced mammary epithelial proliferation and carcinogenesis. Nature 468, 103–107. 10.1038/nature09495. [PubMed: 20881963]
87. Winkler J, Abisoye-Ogunniyan A, Metcalf KJ, and Werb Z. (2020). Concepts of extracellular matrix remodelling in tumour progression and metastasis. Nat Commun 11, 5120. 10.1038/s41467-020-18794-x. [PubMed: 33037194]
88. Mekhdjian AH, Kai F, Rubashkin MG, Prahl LS, Przybyla LM, McGregor AL, Bell ES, Barnes JM, DuFort CC, Ou G, et al. (2017). Integrin-mediated traction force enhances paxillin molecular associations and adhesion dynamics that increase the invasiveness of tumor cells into a three-dimensional extracellular matrix. Mol Biol Cell 28, 1467–1488. 10.1091/mbc.E16-09-0654. [PubMed: 28381423]
89. Wei SC, Fattet L, Tsai JH, Guo Y, Pai VH, Majeski HE, Chen AC, Sah RL, Taylor SS, Engler AJ, and Yang J. (2015). Matrix stiffness drives epithelial-mesenchymal transition and tumour metastasis through a TWIST1-G3BP2 mechanotransduction pathway. Nat Cell Biol 17, 678–688. 10.1038/ncb3157. [PubMed: 25893917]
90. Barnes JM, Kaushik S, Bainer RO, Sa JK, Woods EC, Kai F, Przybyla L, Lee M, Lee HW, Tung JC, et al. (2018). A tension-mediated glycocalyx-integrin feedback loop promotes mesenchymal-like glioblastoma. Nat Cell Biol 20, 1203–1214. 10.1038/s41556-018-0183-3. [PubMed: 30202050]
91. Gilbert PM, Havenstrite KL, Magnusson KE, Sacco A, Leonardi NA, Kraft P, Nguyen NK, Thrun S, Lutolf MP, and Blau HM (2010). Substrate elasticity regulates skeletal muscle stem cell self-renewal in culture. Science 329, 1078–1081. 10.1126/science.1191035. [PubMed: 20647425]
92. Cosgrove BD, Gilbert PM, Porpiglia E, Mourkioti F, Lee SP, Corbel SY, Llewellyn ME, Delp SL, and Blau HM (2014). Rejuvenation of the muscle stem cell population restores strength to injured aged muscles. Nat Med 20, 255–264. 10.1038/nm.3464. [PubMed: 24531378]
93. Cozzolino AM, Noce V, Battistelli C, Marchetti A, Grassi G, Cicchini C, Tripodi M, and Amicone L. (2016). Modulating the Substrate Stiffness to Manipulate Differentiation of Resident Liver Stem Cells and to Improve the Differentiation State of Hepatocytes. Stem Cells Int 2016, 5481493. 10.1155/2016/5481493.
94. Lozoya OA, Wauthier E, Turner RA, Barbier C, Prestwich GD, Guilak F, Superfine R, Lubkin SR, and Reid LM (2011). Regulation of hepatic stem/progenitor phenotype by microenvironment stiffness in hydrogel models of the human liver stem cell niche. Biomaterials 32, 7389–7402. 10.1016/j.biomaterials.2011.06.042. [PubMed: 21788068]
95. Taddei I, Deugnier MA, Faraldo MM, Petit V, Bouvard D, Medina D, Fassler R, Thiery JP, and Glukhova MA (2008). Beta1 integrin deletion from the basal compartment of the mammary epithelium affects stem cells. Nat Cell Biol 10, 716–722. 10.1038/ncb1734. [PubMed: 18469806]
96. Luo M, Zhao X, Chen S, Liu S, Wicha MS, and Guan JL (2013). Distinct FAK activities determine progenitor and mammary stem cell characteristics. Cancer Res 73, 5591–5602. 10.1158/0008-5472.CAN-13-1351. [PubMed: 23832665]
97. Visvader JE, and Stingl J. (2014). Mammary stem cells and the differentiation hierarchy: current status and perspectives. Genes Dev 28, 1143–1158. 10.1101/gad.242511.114. [PubMed: 24888586]

98. Bhat V, Lee-Wing V, Hu P, and Raouf A. (2019). Isolation and characterization of a new basal-like luminal progenitor in human breast tissue. Stem Cell Res Ther 10, 269. 10.1186/s13287-019-1361-3. [PubMed: 31443683]

99. Ataca D, Aouad P, Constantin C, Laszlo C, Beleut M, Shamseddin M, Rajaram RD, Jeitziner R, Mead TJ, Caikovski M, et al. (2020). The secreted protease Adamts18 links hormone action to activation of the mammary stem cell niche. Nat Commun 11, 1571. 10.1038/s41467-020-15357-y. [PubMed: 32218432]

100. Hosseini H, Obradovic MMS, Hoffmann M, Harper KL, Sosa MS, Werner-Klein M, Nanduri LK, Werno C, Ehrl C, Maneck M, et al. (2016). Early dissemination seeds metastasis in breast cancer. Nature 540, 552–558. 10.1038/nature20785. [PubMed: 27974799]

101. Reyes ME, Fujii T, Branstetter D, Krishnamurthy S, Masuda H, Wang X, Reuben JM, Woodward WA, Edwards BJ, Hortobagyi GN, et al. (2017). Poor prognosis of patients with triple-negative breast cancer can be stratified by RANK and RANKL dual expression. Breast Cancer Res Treat 164, 57–67. 10.1007/s10549-017-4233-5. [PubMed: 28417335]

102. Nolan E, Vaillant F, Branstetter D, Pal B, Giner G, Whitehead L, Lok SW, Mann GB, Kathleen Cuningham Foundation Consortium for Research into Familial Breast, C., Rohrbach K, et al. (2016). RANK ligand as a potential target for breast cancer prevention in BRCA1-mutation carriers. Nat Med 22, 933–939. 10.1038/nm.4118. [PubMed: 27322743]

103. Pfitzner BM, Branstetter D, Loibl S, Denkert C, Lederer B, Schmitt WD, Dombrowski F, Werner M, Rudiger T, Dougall WC, and von Minckwitz G. (2014). RANK expression as a prognostic and predictive marker in breast cancer. Breast Cancer Res Treat 145, 307–315. 10.1007/s10549-014-2955-1. [PubMed: 24737168]

104. Toriola AT, Appleton CM, Zong X, Luo J, Weilbaecher K, Tamimi RM, and Colditz GA (2018). Circulating Receptor Activator of Nuclear Factor-kappaB (RANK), RANK ligand (RANKL), and Mammographic Density in Premenopausal Women. Cancer Prev Res (Phila) 11, 789–796. 10.1158/1940-6207.CAPR-18-0199. [PubMed: 30352839]

105. Palafox M, Ferrer I, Pellegrini P, Vila S, Hernandez-Ortega S, Urruticoechea A, Climent F, Soler MT, Munoz P, Vinals F, et al. (2012). RANK induces epithelial-mesenchymal transition and stemness in human mammary epithelial cells and promotes tumorigenesis and metastasis. Cancer Res 72, 2879–2888. 10.1158/0008-5472.CAN-12-0044. [PubMed: 22496457]

106. Huo CW, Chew G, Hill P, Huang D, Ingman W, Hodson L, Brown KA, Magenau A, Allam AH, McGhee E, et al. (2015). High mammographic density is associated with an increase in stromal collagen and immune cells within the mammary epithelium. Breast Cancer Res 17, 79. 10.1186/s13058-015-0592-1. [PubMed: 26040322]

107. Gonzalez-Suarez E, and Sanz-Moreno A. (2016). RANK as a therapeutic target in cancer. FEBS J 283, 2018–2033. 10.1111/febs.13645. [PubMed: 26749530]

108. Tan W, Zhang W, Strasner A, Grivennikov S, Cheng JQ, Hoffman RM, and Karin M. (2011). Tumour-infiltrating regulatory T cells stimulate mammary cancer metastasis through RANKL-RANK signalling. Nature 470, 548–553. 10.1038/nature09707. [PubMed: 21326202]

109. Gomez-Aleza C, Nguyen B, Yoldi G, Ciscar M, Barranco A, Hernandez-Jimenez E, Maetens M, Salgado R, Zafeiroglou M, Pellegrini P, et al. (2020). Inhibition of RANK signaling in breast cancer induces an anti-tumor immune response orchestrated by CD8+ T cells. Nat Commun 11, 6335. 10.1038/s41467-020-20138-8. [PubMed: 33303745]

110. Ahern E, Harjunpaa H, O'Donnell JS, Allen S, Dougall WC, Teng MWL, and Smyth MJ (2018). RANKL blockade improves efficacy of PD1-PD-L1 blockade or dual PD1-PD-L1 and CTLA4 blockade in mouse models of cancer. Oncoimmunology 7, e1431088. 10.1080/2162402X.2018.1431088.

111. Yoldi G, Pellegrini P, Trinidad EM, Cordero A, Gomez-Miragaya J, Serra-Musach J, Dougall WC, Munoz P, Pujana MA, Planelles L, and Gonzalez-Suarez E. (2016). RANK Signaling Blockade Reduces Breast Cancer Recurrence by Inducing Tumor Cell Differentiation. Cancer Res 76, 5857–5869. 10.1158/0008-5472.CAN-15-2745. [PubMed: 27480274]

112. Davie SA, Maglione JE, Manner CK, Young D, Cardiff RD, MacLeod CL, and Ellies LG (2007). Effects of FVB/NJ and C57Bl/6J strain backgrounds on mammary tumor phenotype in inducible nitric oxide synthase deficient mice. Transgenic Res 16, 193–201. 10.1007/s11248-006-9056-9. [PubMed: 17206489]

113. Aupperlee MD, Drolet AA, Durairaj S, Wang W, Schwartz RC, and Haslam SZ (2009). Strain-specific differences in the mechanisms of progesterone regulation of murine mammary gland development. Endocrinology 150, 1485–1494. 10.1210/en.2008-1459. [PubMed: 18988671]

114. Wagner KU, Wall RJ, St-Onge L, Gruss P, Wynshaw-Boris A, Garrett L, Li M, Furth PA, and Hennighausen L. (1997). Cre-mediated gene deletion in the mammary gland. Nucleic Acids Res 25, 4323–4330. 10.1093/nar/25.21.4323. [PubMed: 9336464]

115. Muller WJ, Sinn E, Pattengale PK, Wallace R, and Leder P. (1988). Single-step induction of mammary adenocarcinoma in transgenic mice bearing the activated c-neu oncogene. Cell 54, 105–115. 10.1016/0092-8674(88)90184-5. [PubMed: 2898299]

116. Livet J, Weissman TA, Kang H, Draft RW, Lu J, Bennis RA, Sanes JR, and Lichtman JW (2007). Transgenic strategies for combinatorial expression of fluorescent proteins in the nervous system. Nature 450, 56–62. 10.1038/nature06293. [PubMed: 17972876]

117. Rios AC, Fu NY, Lindeman GJ, and Visvader JE (2014). In situ identification of bipotent stem cells in the mammary gland. Nature 506, 322–327. 10.1038/nature12948. [PubMed: 24463516]

118. Hsu H, Lacey DL, Dunstan CR, Solovyev I, Colombero A, Timms E, Tan HL, Elliott G, Kelley MJ, Sarosi I, et al. (1999). Tumor necrosis factor receptor family member RANK mediates osteoclast differentiation and activation induced by osteoprotegerin ligand. Proc Natl Acad Sci U S A 96, 3540–3545. 10.1073/pnas.96.7.3540. [PubMed: 10097072]

119. Bhagwat SV, McMillen WT, Cai S, Zhao B, Whitesell M, Shen W, Kindler L, Flack RS, Wu W, Anderson B, et al. (2020). ERK Inhibitor LY3214996 Targets ERK Pathway-Driven Cancers: A Therapeutic Approach Toward Precision Medicine. Mol Cancer Ther 19, 325–336. 10.1158/1535-7163.MCT-19-0183. [PubMed: 31744895]

120. Bankhead P, Loughrey MB, Fernandez JA, Dombrowski Y, McArt DG, Dunne PD, McQuaid S, Gray RT, Murray LJ, Coleman HG, et al. (2017). QuPath: Open source software for digital pathology image analysis. Sci Rep 7, 16878. 10.1038/s41598-017-17204-5. [PubMed: 29203879]

121. Schindelin J, Arganda-Carreras I, Frise E, Kaynig V, Longair M, Pietzsch T, Preibisch S, Rueden C, Saalfeld S, Schmid B, et al. (2012). Fiji: an open-source platform for biological-image analysis. Nat Methods 9, 676–682. 10.1038/nmeth.2019. [PubMed: 22743772]

122. Varghese F, Bukhari AB, Malhotra R, and De A. (2014). IHC Profiler: an open source plugin for the quantitative evaluation and automated scoring of immunohistochemistry images of human tissue samples. PLoS One 9, e96801. 10.1371/journal.pone.0096801. [PubMed: 24802416]

123. Shackleton M, Vaillant F, Simpson KJ, Stingl J, Smyth GK, Asselin-Labat ML, Wu L, Lindeman GJ, and Visvader JE (2006). Generation of a functional mammary gland from a single stem cell. Nature 439, 84–88. 10.1038/nature04372. [PubMed: 16397499]

124. Hu Y, and Smyth GK (2009). ELDA: extreme limiting dilution analysis for comparing depleted and enriched populations in stem cell and other assays. J Immunol Methods 347, 70–78. 10.1016/j.jim.2009.06.008. [PubMed: 19567251]

125. Shepherd JA, Herve L, Landau J, Fan B, Kerlikowske K, and Cummings SR (2006). Clinical comparison of a novel breast DXA technique to mammographic density. Med Phys 33, 1490–1498. 10.1118/1.2193691. [PubMed: 16752583]

126. Shepherd JA, Kerlikowske K, Ma L, Duewer F, Fan B, Wang J, Malkov S, Vittinghoff E, and Cummings SR (2011). Volume of mammographic density and risk of breast cancer. Cancer Epidemiol Biomarkers Prev 20, 1473–1482. 10.1158/1055-9965.EPI-10-1150. [PubMed: 21610220]

127. Johnson KR, Leight JL, and Weaver VM (2007). Demystifying the effects of a three-dimensional microenvironment in tissue morphogenesis. Methods Cell Biol 83, 547–583. 10.1016/S0091-679X(07)83023-8. [PubMed: 17613324]

128. Przybyla L, Lakins JN, Sunyer R, Trepat X, and Weaver VM (2016). Monitoring developmental force distributions in reconstituted embryonic epithelia. Methods 94, 101–113. 10.1016/j.ymeth.2015.09.003. [PubMed: 26342256]

129. Lakins JN, Chin AR, and Weaver VM (2012). Exploring the link between human embryonic stem cell organization and fate using tension-calibrated extracellular matrix functionalized polyacrylamide gels. Methods Mol Biol 916, 317–350. 10.1007/978-1-61779-980-8_24. [PubMed: 22914951]

130. Kline RB (2023). Principles and practice of structural equation modeling, Fifth edition. Edition (The Guilford Press).

HIGHLIGHTS

- Integrin mechanosignaling expands mammary epithelial stem-progenitors
- Mechanosensitive ERK-PR promotes RANK signaling to expand stem-progenitor cells
- Mechanosignaling and RANK-driven stem-progenitor expansion enhance tumor initiation
- Patients with dense breasts exhibit integrin/ERK/PR/RANKL-induced stemness

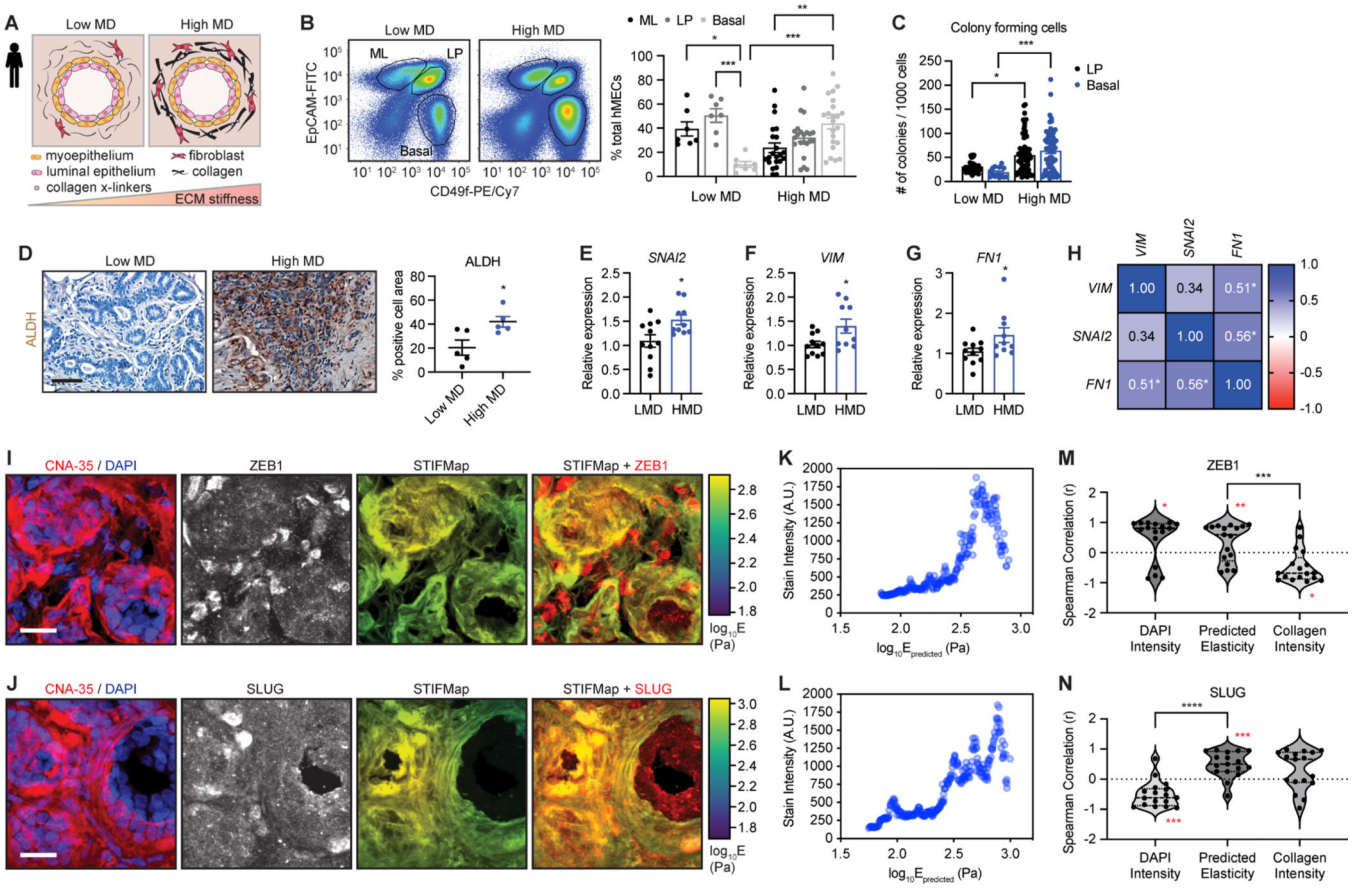

Figure 1. Extracellular matrix stiffness associates with frequency of mesenchymal human mammary epithelial progenitor cells

(A) Cartoon: human breast tissue with low and high mammographic density (MD).

(B) (left) Representative plots showing FACS analysis of human breast tissues (n=7; low MD, n=22; high MD, biological replicates). (right) Graph illustrating average percentage of mature luminal (ML), luminal progenitor (LP) and basal MECs.

(C) FACS isolated (n=7; low MD, n=22; high MD, biological replicates) LP and Basal MECs were subjected to colony formation assays in rBM to assess progenitor activity. Graph includes all technical repeats and shows average colonies/1000 cells.

(D) (left) Immunohistochemistry of low MD and high MD (n=5 biological replicates) breast tissues with ALDH antibody. Nuclei are counterstained with hematoxylin. Scale bar, 50 μm. (right) Graph shows average percent positive ALDH staining/cell area.

(E-G) qRT-PCR analysis of relative gene expression (normalized to *Krt8*) for the indicated genes in human breast tissues (n=11; low MD, n=10; high MD, biological replicates).

(**H**) Correlation matrix comparing individual patient values for the qRT-PCR analyses from (E-G). Red-to-blue scale indicates negative-to-positive Pearson correlation (n=21).

(I and J) (left) Representative immunofluorescence images of human breast tissues stained for collagen (CNA-35, red) and nuclei (DAPI, blue), (center left) ZEB1 (I) or SLUG (J). (center right) Predicted matrix elasticity “collagen paint” (STIFMap, viridis) and (right) an overlay of STIFMap and ZEB1 or SLUG staining. Scale bar, 20 μm.

(K and L) Scatterplots of STIFMap intensity (log ($E_{predicted}$)) versus ZEB1 (K) or SLUG (L) stain intensity for each pixel in (I and J) indicating the 99^{th} percentile of stain intensity for each STIFMap percentile.

(M and N) Violin plots of the Spearman correlation for each field-of-view comparing the 99^{th} percentile of ZEB1 (M) or SLUG (N) staining intensity versus percentiles of collagen stain intensity, predicted elasticity, or DAPI stain intensity. Internal bars indicate a Box-plot with median and interquartile range (n=5–6 biological replicates; 17 individual regions). Graphs are represented as mean +/− S.E.M with the exception of K and N as indicated. Statistical tests used were 2-way ANOVA with Tukey's multiple comparisons test (B, C), unpaired *t*-test (D-G), Pearson's correlation (H), Wilcoxon signed-rank test (* in red, K, N) and Mann-Whitney test (K, N), *P<0.05, **P<0.005, ***P<0.0005, ns=non-significant.

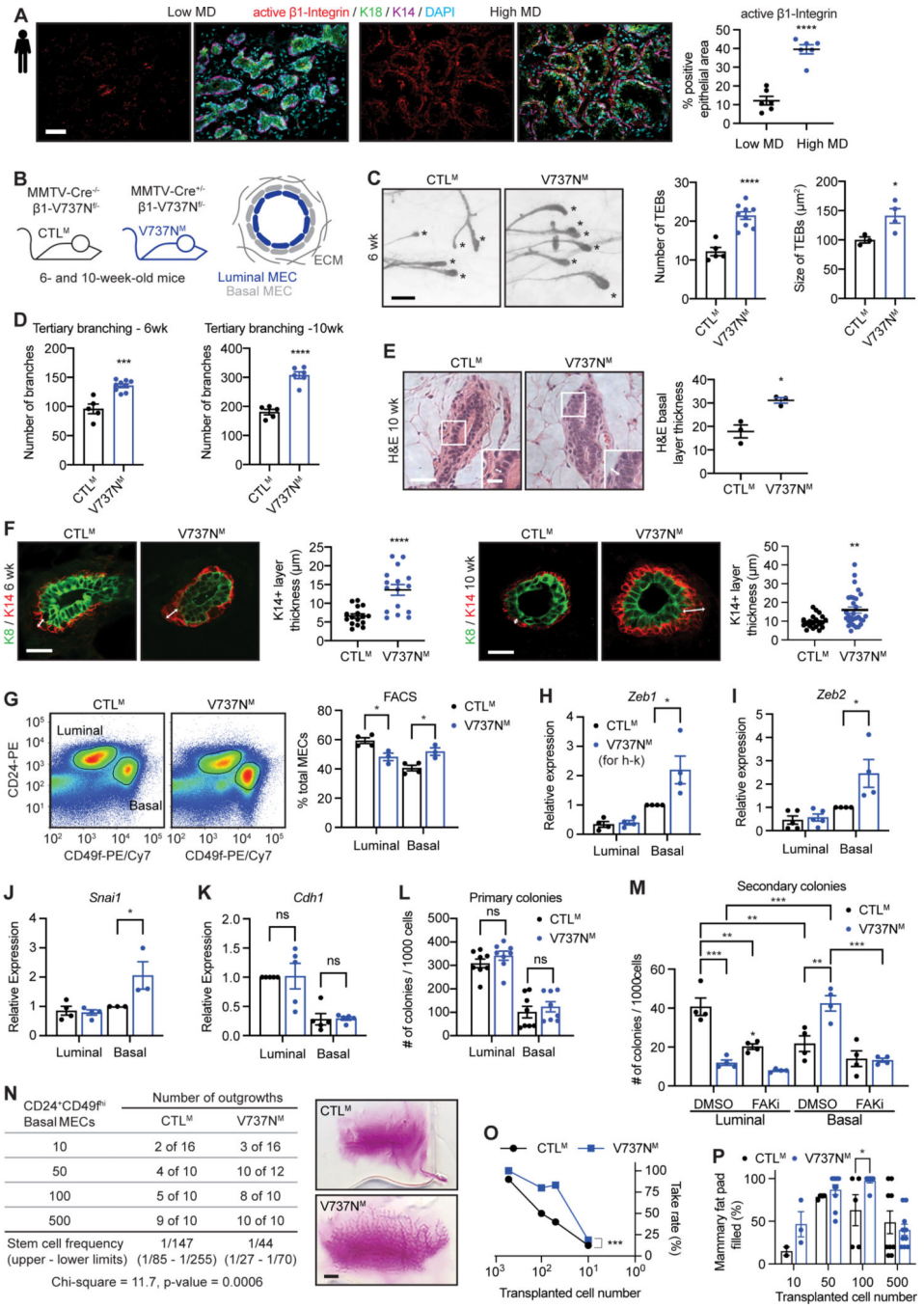

Figure 2. Mechanosignaling in luminal mammary epithelial cells fosters stem/progenitor activity

(A) (left) Representative immunofluorescence for human breast tissues (n=6 biological replicates each; low and high MD) with antibodies to active β1-integrin (red), Keratin 18 (K18, green) and Keratin 14 (K14, magenta). Nuclei are stained with DAPI (cyan). Scale bar, 50 μm. (right) Graph shows average percentage of positive active β1-integrin staining/ epithelial cell area.

(B) Cartoons illustrating control mice (CTL^M) and mice expressing V737N-β1-integrin ($V737N^M$) with the predicted V737N-expression in a ductal cross-section (blue).

(C) (left) Representative H&E-stained mammary gland wholemounts. Scale bar, 400 μm. (middle and right) Graphs showing the average number and size of terminal end buds (TEBs) (CTL^M; n=3–5, $V737N^M$; n=4–9 biological replicates). Asterisks indicate TEBs.
(D) Graphs showing average tertiary ductal branches observed for CTL^M and $V737N^M$ mice at 6-(left) and 10- (right) weeks of age (n=5–9 biological replicates).
(E) (left) Representative H&E-stained mammary gland sections from 10-week-old mice. Scale bars, 50 μm. White double-sided arrows demarcate basal MEC layer thickness (inset). (right) Graph shows average thickness of the basal/myoepithelial layer (CTL^M and $V737N^M$; n=3 biological replicates).
(F) Representative immunofluorescence of luminal and basal cytokeratins (K8; green and K14; red) for mammary glands from CTL^M and $V737N^M$ mice (n=5 biological replicates each) at 6-(left) and 10- (center right) weeks of age. White double-sided arrows demarcate K14-positive basal layer thickness. Scale bar, 50 μm. Graphs show average thickness of K14-postive layers for mice at 6- (center left) and 10- (right) weeks of age.
(G) (left) Representative FACS of mammary epithelial lineages. (right) The average percentages of luminal and basal populations are plotted (CTL^M; n=4, $V737N^M$; n=3 biological replicates).
(H-K) RNA was isolated from luminal and basal MECs sorted from CTL^M and $V737N^M$ mice (n=4–6 biological replicates). Graphs show relative expression for the indicated genes.
(L and M) MECs sorted as in (G) were subjected to primary and secondary rBM colony formation assays (n=8; primary colony, n=4; secondary colony, biological replicates). (M) shows secondary colony formation in the presence of vehicle (DMSO) or FAK-inhibitor (FAKi; PND1186).
(N) Limiting dilution transplantation assays were performed with basal ($CD24^+$; $CD49f^{hi}$) MECs sorted as in (G). (right) Representative images of carmine alum-stained epithelial transplants. Scale bar, 2 mm.
O) The data from (N) plotted as percentage of mammary gland repopulating events (take rate) against transplanted cell number.
(**P**) A comparison of the extent of fat pad repopulation from (N) at each transplanted cell number.
Graphs are represented as mean +/− S.E.M. Statistical tests used were unpaired *t*-test (A, C, D-F), 2-way ANOVA with Tukey's multiple comparisons test (G-M, P) and score test for differences in stem cell frequencies (N and O), *P<0.05, **P<0.005, ***P<0.0005, ns=non-significant.

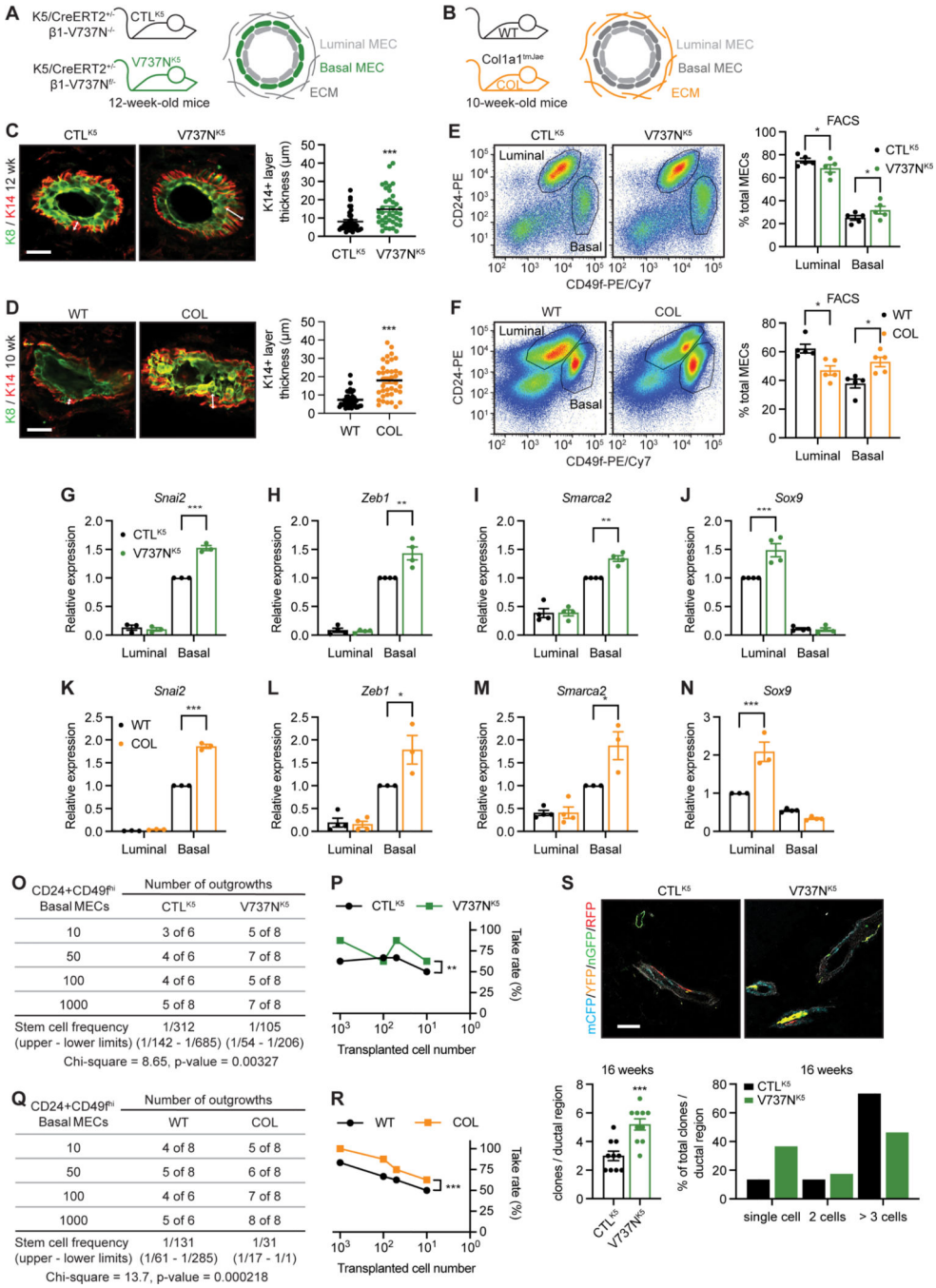

Figure 3. Mechanosignaling in basal mammary epithelial cells and increased stromal collagen density foster stem/progenitor activity

(A) Cartoons illustrating control mice (CTL^{K5}) and mice expressing V737N-β1-integrin ($V737N^{K5}$) with the predicted V737N-expression in a ductal cross-section (green).

(B) Cartoons illustrating wildtype (WT) and Collagenase-resistant Collagen I-expressing mice (COL) with increased ECM density around mammary epithelial ducts (orange).

(C and D) (left) Representative immunofluorescence of luminal and basal cytokeratins (K8; green and K14; red) for mammary glands from CTL^{K5} and $V737N^{K5}$ mice (C, n=5

biological replicates each) at 12-weeks of age and WT and COL mice (D, n=5 biological replicates each) at 10-weeks of age. Scale bar, 20 μm. (right) White double-sided arrows indicate K14-positive basal layer thickness. Graphs show the average thickness of K14-postive layers for the indicated mice.

(E and F) (left) Representative FACS for mammary epithelial lineages from CTL^{K5} and $V737N^{K5}$ mice (E) and WT and COL mice (F). (right) The average percentages of luminal and basal epithelial populations are plotted (n=5 biological replicates each).

(G-J) RNA was isolated from MECs sorted as in (E) from CTL^{K5} and $V737N^{K5}$ mice (n=3–4 biological replicates). Graphs showing relative expression for the indicated genes are displayed.

(K-N) RNA was isolated from WT and COL mice as in (G-J) (n=3–4 biological replicates). Graphs showing relative expression for the indicated genes are displayed.

(O) Limiting dilution transplantation assays (LDTAs) were performed with basal ($CD24^{+}$; $CD49f^{hi}$) MECs sorted from CTL^{K5} and $V737N^{K5}$ mice. Stem cell frequency was calculated from the number of mammary gland repopulating events.

(P) The data from (O) plotted as percentage of mammary gland repopulating events (take rate) against the transplanted cell number.

(Q) LDTAs were performed for WT and COL mice as in (O).

(R) The data from (Q) plotted as in (P).

(S) Tamoxifen inducible lineage tracing of MECs in CTL^{K5} and $V737N^{K5}$ mammary glands (n=3 biological replicates each). (top) Representative images of mammary glands 16-weeks post tamoxifen induction. Scale bar, 50 μm. Frequency of distinct fluorescent clones per ductal region (bottom left) and the relative percentage of single cell, two-cell, and multicellular clones (bottom right) are represented as bar plots.

Graphs are represented as mean +/− S.E.M. Statistical tests used were unpaired *t*-test (C, D and S), 2-way ANOVA with Šídák's multiple comparisons test (E, F), 2-way ANOVA with Tukey's multiple comparisons test (G-N) and score test for differences in stem cell frequencies (O-R), *P<0.05, **P<0.005, ***P<0.0005, ns=non-significant.

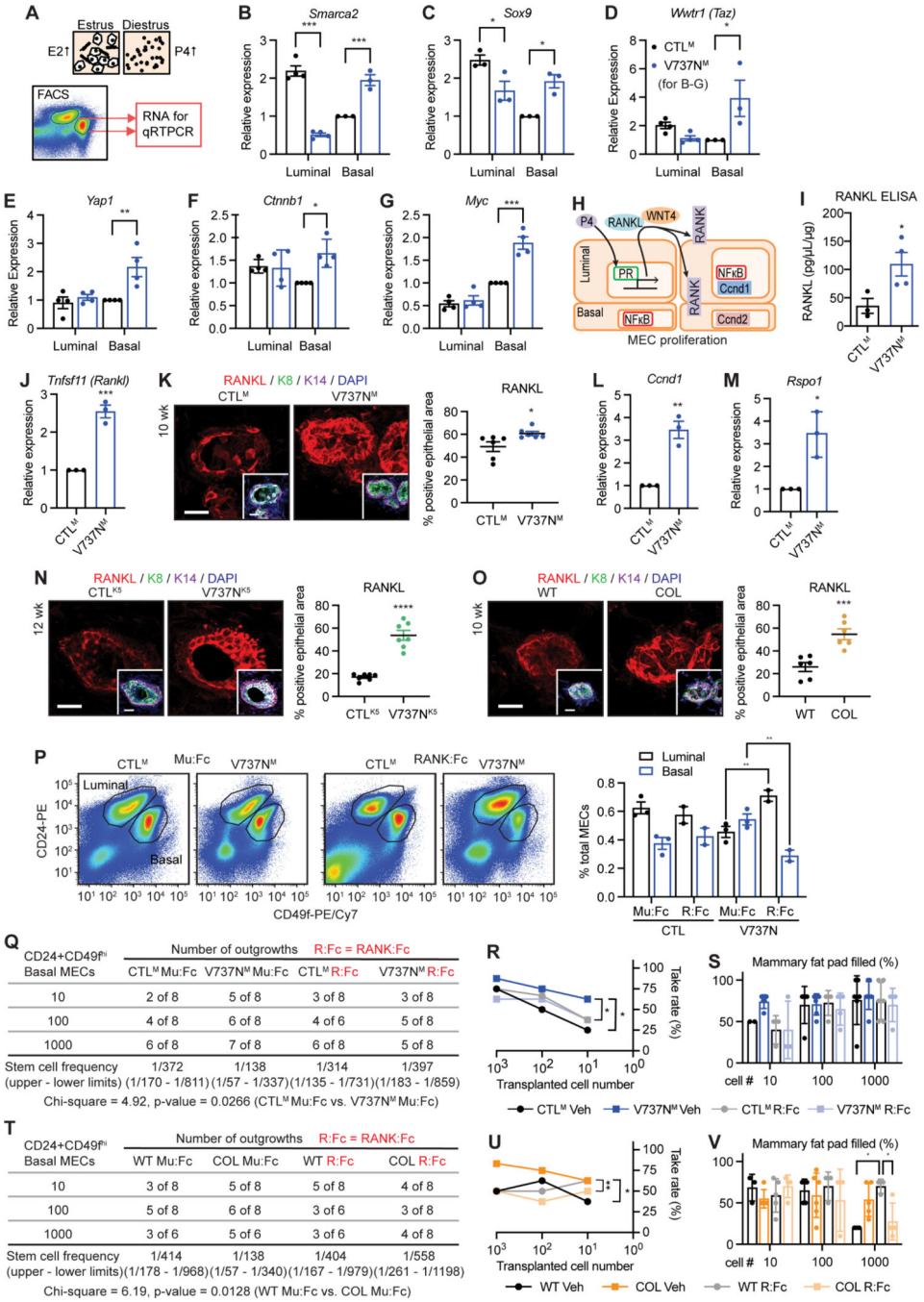

Figure 4. Mechanosensitive mammary stem-progenitor cell expansion is driven by hormone-induced RANK signaling

(A) Cartoon: cytology used to determine stages of the estrus cycle (E2=estrogen; P4=progesterone) in mice prior to FACS-mediated isolation of MECs for RNA extraction and qRT-PCR.

(B-G) Graphs showing qRT-PCR analysis of relative gene expression for the indicated genes using cells sorted as in (A) (n=3–4 biological replicates).

(H) Cartoon: P4 stimulates progesterone receptor (PR)-mediated transcription of paracrine factors, RANKL and WNT4, to stimulate NFκB activity and MEC proliferation.
(I) Whole mammary gland lysates were subjected to ELISA to measure RANKL levels (CTL^M; n=3, $V737N^M$; n=4 biological replicates).
(J) Graph showing qRT-PCR analysis of gene expression for *Tnfsf11 (Rankl)* in MECs sorted as in (A) (n=3–4 biological replicates).
(K) (left) Representative immunofluorescence of mammary gland tissues (n=6 biological replicates each, CTL^M and $V737N^M$) with antibodies specific for RANKL (red), Keratin 8 (K8, green) and Keratin 14 (K14, magenta). Nuclei are stained with DAPI (blue, inset). Scale bars, 50 μm. (right) Graph shows average percentage of positive RANKL staining/MEC area.
(L and M) Graphs showing qRT-PCR analysis of gene expression for *Ccnd1* (L) and *Rspo1* (M) in MECs sorted as in (A) (n=3 biological replicates).
(N and O) (left) Representative immunofluorescence of mammary gland tissues and quantification as in (K) for CTL^{K5} and $V737N^{K5}$ mice (N, n=7 biological replicates each) and WT and COL mice (O; n=6 biological replicates each).
MECs were isolated by FACS from CTL^M and $V737N^M$ mice that were treated with RANK:Fc or Murine:Fc (Mu:Fc). Representative FACS plots are shown and the average percentage of luminal and basal MECs are plotted (n=2–3 biological replicates).
(Q) Limiting dilution transplantation assays (LDTAs) were performed with basal ($CD24^+$; $CD49f^{hi}$) MECs sorted from CTL^M and $V737N^M$ mice treated as in (P). Stem cell frequency was calculated from the number of mammary gland repopulating events. Data not noted: CTL Mu:Fc vs. $V737N^M$ R:Fc, P = 0.0143.
(R) The data from (Q) plotted as percentage of mammary gland repopulating events (take rate) against transplanted cell number.
(S) A comparison of the extent of fat pad repopulation from (Q) at each transplanted cell number.
(T) LDTAs were performed and analyzed as in (Q) for WT and COL mice. Data not noted: COL Mu:Fc vs. WT R:Fc, P = 0.0152, and COL Mu:Fc vs. COL R:Fc, P = 0.00157.
(U and V) The data from (T) plotted as in (R and S).
Graphs are represented as mean +/− S.E.M. Statistical tests used were 2-way ANOVA with Tukey's multiple comparisons test (B-G, P, S and V), unpaired *t*-test (I-O) and score test for differences in stem cell frequencies (Q-R and T-U), *P<0.05, **P<0.005, ***P<0.0005, ns=non-significant.

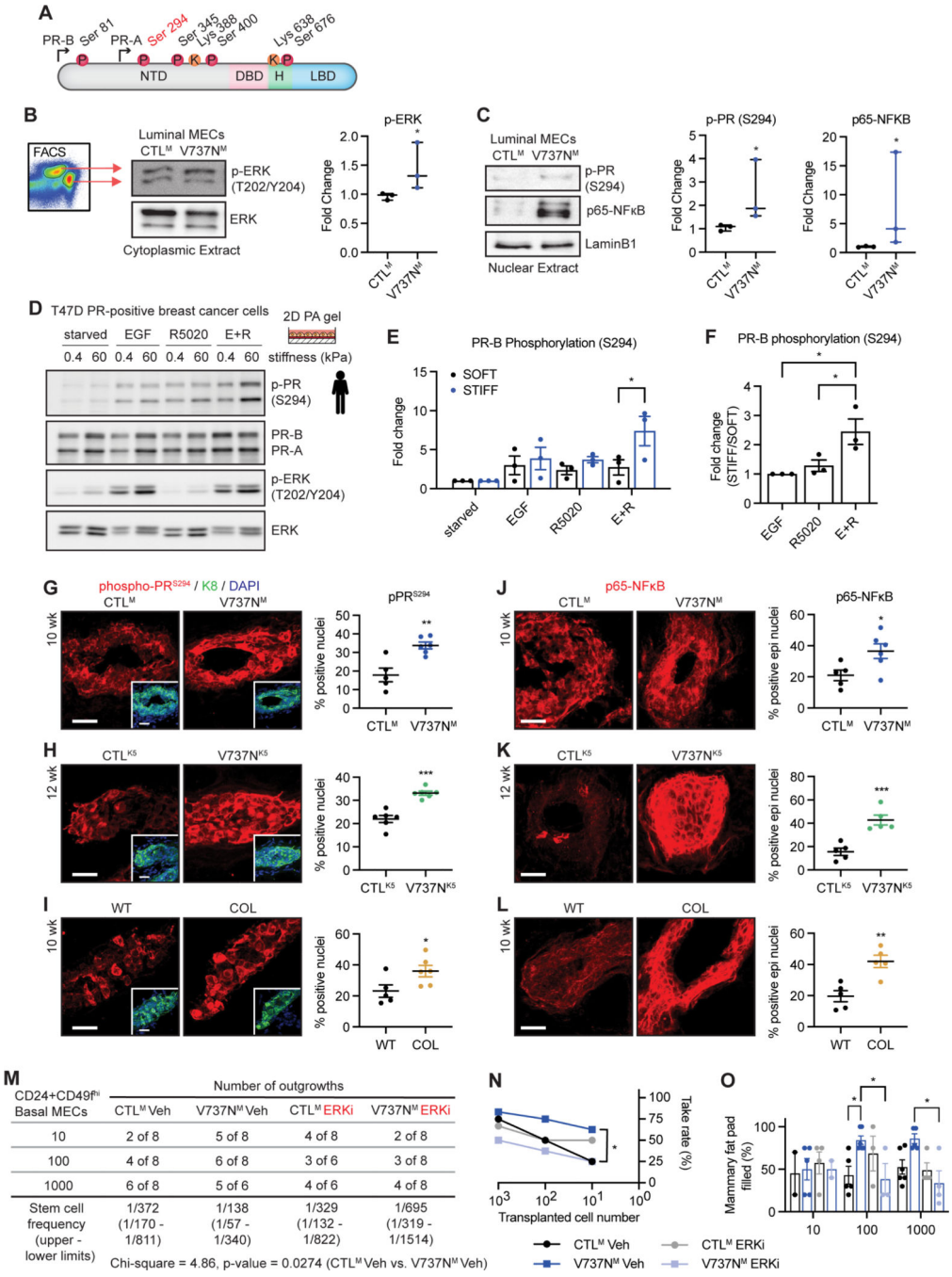

Figure 5. Matrix stiffness and mechanosignaling potentiate progesterone signaling

(A) Cartoon: progesterone receptor (PR) isoforms with sites of post-translational modification (P=phosphorylation, K=SUMOylation/acetylation).

(B) MECs were isolated by FACS as in Figure 2G and fractionated to prepare nuclear and cytoplasmic lysates. (left) Cytoplasmic fractions were subjected to immunoblotting with antibodies specific to phospho-ERK (p-ERK; T202/Y204) and total ERK. (right) Densitometry for phospho-ERK:total ERK is plotted (3 biological replicates).

(C) (left) Nuclear lysate fractions from (B) were subjected to immunoblotting with antibodies to phosphorylated PR (p-PR, S294), p65-NFκB and Lamin B1. Densitometry for p-PR:Lamin B1 (S294; middle), and p65-NFκB:Lamin B1 (right) are plotted (3 biological replicates each).

(D) T47D breast cancer cells were cultured on ECMs with varied stiffness (0.4 and 60 kPa), serum starved, and treated with EGF, R5020, or EGF and R5020 together (E+R) for 15 min. Cells were lysed for immunoblotting with antibodies to phospho-PR (S294), total PR, phospho-ERK (p-ERK; T202/Y204) and ERK.

(E) Graph showing densitometry for PR-B phosphorylation:total PR-B from three biological replicates conducted as in (D). Treatments were normalized to the non-treated serum-starved condition.

(F) Data from (D) plotted as fold change (STIFF/SOFT).

(G-I) (left) Representative immunofluorescence for mammary gland tissues with antibodies for phospho-PR^{S294} (red) and Keratin 8 (K8; green, inset). Nuclei are stained with DAPI (blue, inset). Scale bars, 50 μm. (right) Graphs show the average percentage of K8-positive cell nuclei also positive for phospho-PR^{S294} (top, G: CTL^{M}, n=5 and $V737N^{M}$, n=6; center, H: CTL^{K5}, n=6 and $V737N^{K5}$, n=6; bottom, WT, n=5 and COL, n=6 biological replicates).

(J-L) (left) Representative immunofluorescence for mammary gland tissues with an antibody to p65-NFκB (red). Scale bar, 50 μm. (right) Graphs show the average percentage of epithelial cell nuclei positive for p65-NFκB (top, G: CTL^{M}, n=5 and $V737N^{M}$, n=6; center, H: CTL^{K5}, n=5 and $V737N^{K5}$, n=5; bottom, WT, n=5 and COL, n=5 biological replicates).

(M) Limiting dilution transplantation assays were performed with basal ($CD24^{+}$; $CD49f^{hi}$) MECs sorted from CTL^{M} and $V737N^{M}$ mice treated with vehicle or an ERK inhibitor (ERKi). Stem cell frequency was calculated from the number of mammary gland repopulating events. Data not noted: $V737N^{M}$ Veh vs. CTL ERKi, P = 0.0541, and $V737N^{M}$ Veh vs. $V737N^{M}$ ERKi, P = 0.000419.

(N) The data from (M) plotted as percentage of mammary gland repopulating events (take rate) against transplanted cell number.

(O) A comparison of the extent of fat pad repopulation from (M) at each transplanted cell number.

Graphs are represented as mean +/− S.E.M with the exception of B and C which show median, min and max. Statistical tests used were Mann-Whitney test (B and C, one-tailed), 2-way ANOVA with Šídák's multiple comparisons test (E), 2-way ANOVA with Tukey's multiple comparisons test (F, O), unpaired *t*-test (G-L) and score test for differences in stem cell frequencies (M, N), *P<0.05, **P<0.005, ***P<0.0005, ns=non-significant.

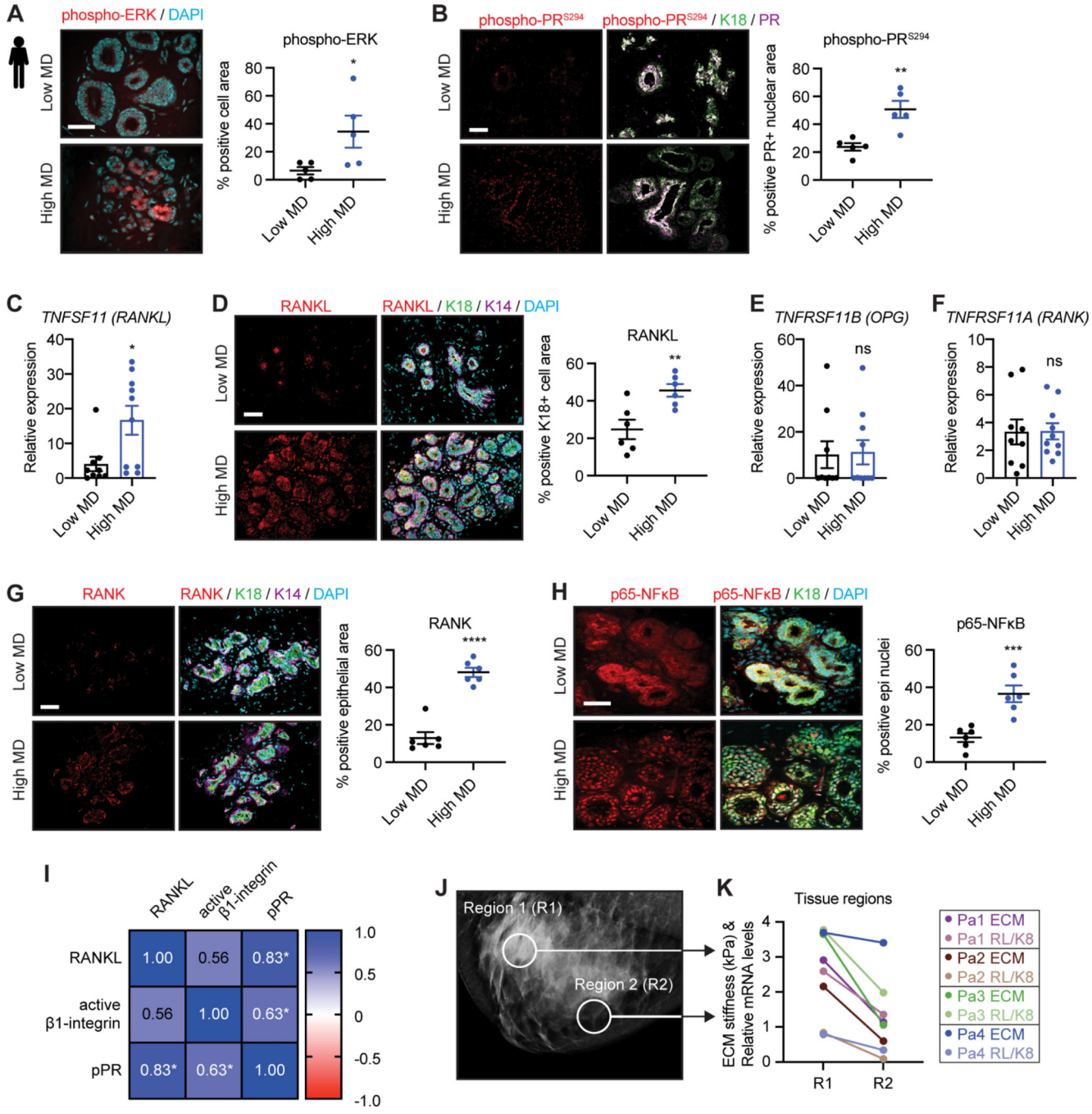

Figure 6. Mammographic density correlates with stromal stiffness and elevated RANK activity

(A and B) (left) Representative immunofluorescence of human breast tissues with antibodies for (A) phospho-ERK (red), and (B) phospho-PR^{S294} (red), Keratin 18 (K18, green) and PR (magenta). Nuclei are stained with DAPI (cyan). Scale bars, 50 μm. (right) Graphs show average percentage of positive phospho-ERK staining per total epithelial cell area (A), and average percentage of PR-positive nuclear area also positive for phospho-PR^{S294} staining (B) (n=5 biological replicates each for low and high MD).

(C) qRT-PCR analysis of gene expression for *TNFSF11 (RANKL)* (normalized to *Krt8*) in human breast tissues (low MD; n=9, high MD; n=10 biological replicates).
(D) (left) Representative immunofluorescence of human breast tissues with antibodies for RANKL (red), Keratin 18 (K18, green) and Keratin 14 (K14, magenta). Nuclei are stained with DAPI (cyan). Scale bar, 50 μm. (right) Graph shows average percentage of K18-positive cell area also positive for RANKL staining (n=6 biological replicates each for low and high MD).
(E and F) qRT-PCR analysis as in (C) for *TNFRS11B (OPG)* and *TNFRSF11A (RANK)* (low MD; n=9, high MD; n=10 biological replicates).
(G and H) (left) Representative immunofluorescence of human breast tissues with antibodies for (G) RANK (red), Keratin 18 (K18, green) and Keratin 14 (K14, magenta), and (H) p65-NFκB (red) and Keratin 18 (K18, green). Nuclei are stained with DAPI (cyan). Scale bars, 50 μm. (right) Graphs show average percentage of positive RANK staining per total epithelial cell area (G), and average percentage of positive nuclear p65-NFκB staining per total epithelial cell nuclei (H) (n=6 biological replicates each for low and high MD).
(I) Correlation matrix comparing immunofluorescence from the same individual patient specimens and the analyses presented in Figures 1A, 6B and 6D (n=8). Red-to-blue scale indicates negative-to-positive Pearson correlation values.
(J) Representative whole breast mammogram where two regions of different mammographic density (MD) were excised for cryo-sectioning and subsequent analysis.
(K) Two regions of the same breast as in (J) were used to measure average ECM stiffness by AFM. Sections of each region were also used to isolate RNA and determine relative *TNFSF11* (*RANKL*) gene expression as in (C). Average AFM measurements and relative *RANKL* expression levels were plotted for each region to display their relationship (n=4 individual patients (Pa1–4)).
Graphs are represented as mean +/− S.E.M. Statistical tests used were unpaired *t*-test (A-H) and Pearson's correlation (I), *P<0.05, **P<0.005, ***P<0.0005, ns=non-significant.

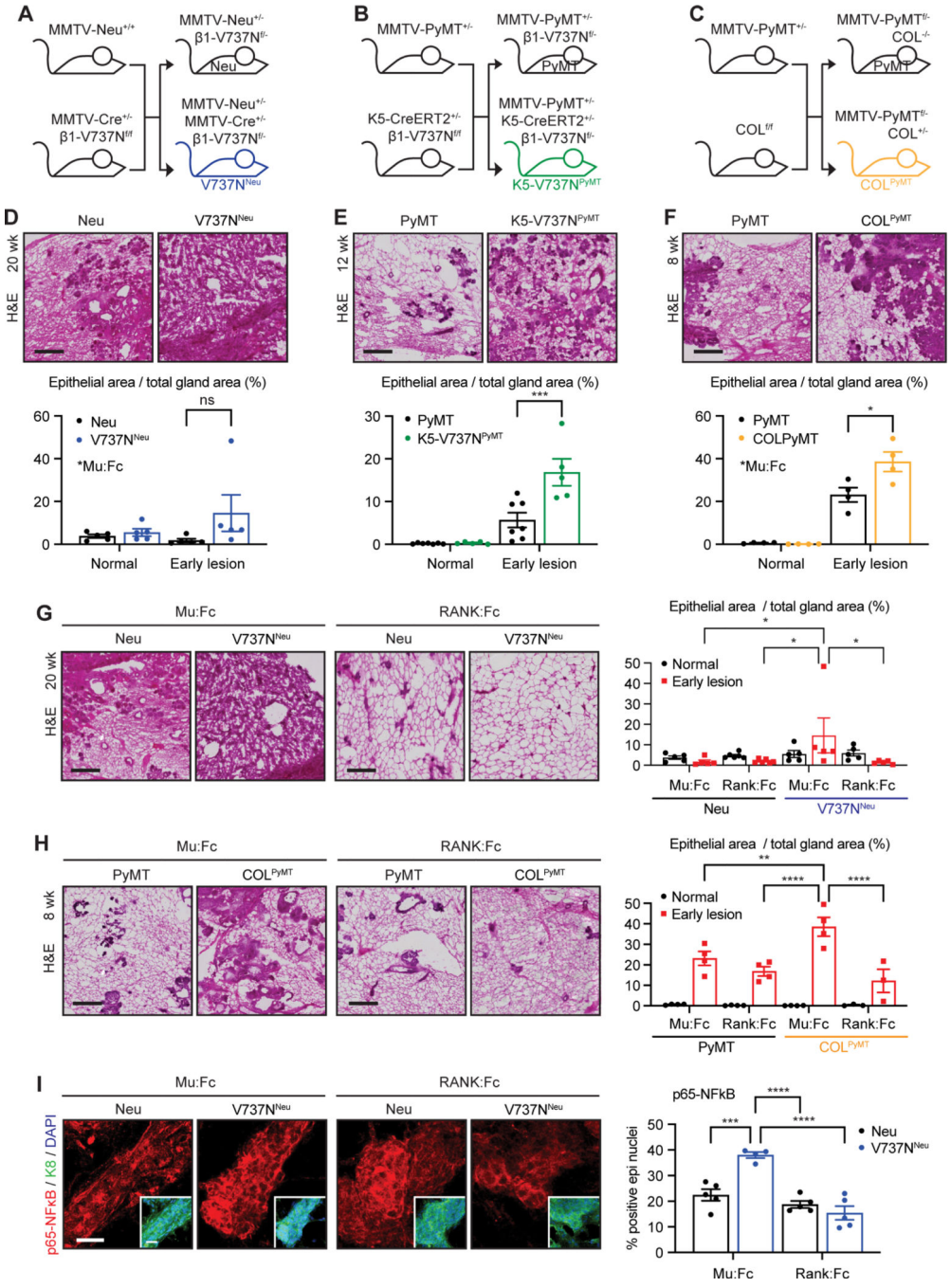

Figure 7. Mechanosignaling-dependent early tumor lesion formation is abrogated by RANKL inhibition

(A-C) Breeding schematics for Neu and V737N^{Neu} (A), PyMT and K5-V737N^{PyMT} (B), and PyMT and COL^{PyMT} (C) transgenic mice.

(D-F) (top) Representative H&E images of mammary gland sections for Murine:Fc treated (Mu:Fc) mice. Scale bar, 400 μm. (bottom) Quantification of average normal ductal and early tumor lesion area per total gland area. (D) Neu and V737N^{Neu} mice (n=5 biological

replicates each), (E) PyMT and K5-V737N^{PyMT} mice (n=7 and n=5 biological replicates), (F) PyMT and COL mice (n=4 biological replicates each).

(G and H) Representative H&E images of mammary gland sections (left) and quantification (right) as in (D-F). Scale bar, 400 μm. (G) Neu and V737N^{Neu} mice, (H) PyMT and COL^{PyMT} mice (n=5 biological replicates each) were also treated with RANK:Fc. Mu:Fc treated mice are the same as those displayed in (D) and (F) for comparison.

(I) (left) Representative immunofluorescence of mammary gland tissues from mice treated as in (G and H) using antibodies to p65-NFκB (red) and Keratin 8 (K8, green, inset). Nuclei are stained with DAPI (blue, inset). Scale bar, 50 μm. (right) Graph shows average percentage of positive nuclear p65-NFκB staining/epithelial cell nuclei (n=5 biological replicates each).

Graphs are represented as mean +/− S.E.M. Statistical tests used were 2-way ANOVA with Tukey's multiple comparisons test (D-I), *P<0.05, **P<0.005, ***P<0.0005, ns=non-significant.

REAGENT or RESOURCE	SOURCE	IDENTIFIER
Antibodies		
E-cadherin	BD Biosciences, clone 36	Cat. #: 610181, RRID:AB_397580
ALDH	BD Biosciences, clone 44	Cat. #: 611194, RRID:AB_2224312
p-Histone H3	Santa Cruz Biotechnology	Cat. #: sc-8656-R, RRID:AB_653256
phospho-p130-Cas (Y410)	Cell Signaling Technology	Cat. #: 4011, RRID:AB_2274823
phospho-FAK (Y397)	Cell Signaling Technology	Cat. #: 8556, RRID:AB_10891442
phospho-FAK (Y397)	Thermo Fischer Scientific, clone 141–9	Cat. #: 44–625G, RRID:AB_2533702
phospho-p44/42 MAPK (ERK1/2) (T202/Y204)	Cell Signaling Technology	Cat. #: 9101, RRID:AB_331646
NFkB p65 (D14E12) XP	Cell Signaling Technology	Cat. #: 8242, RRID:AB_10859369
phospho-Histone H3 (S10)	Cell Signaling Technology	Cat. #: 9701, RRID:AB_331535
cleaved Caspase-3 (Asp175)	Cell Signaling Technology	Cat. #: 9661, RRID:AB_2341188
Integrin β1(activated)	MilliporeSigma, clone HUTS-4	Cat. #: MAB2079Z, RRID:AB_2233964
Integrin β1	MilliporeSigma, clone JB1A	Cat. #: MAB1965, RRID:AB_2128061
CD29 (Integrin b1, activated)	BD Biosciences, clone 9EG7	Cat. #: 553715, RRID:AB_395001
PR	Santa Cruz Biotechnology, clone H-190	Cat. #: sc-7208, RRID:AB_2164331
PR	Thermo Fischer Scientific, clone hPRa7	Cat. #: MA5–12658, RRID:AB_11000632
ERα	Abcam	Cat. #: ab37438, RRID:AB_732246
Alexa Fluor (AF)488 Keratin 8	Abcam, clone EP1628Y	Cat. #: ab192467, RRID:AB_2864346
Keratin 14 (K14)	Covance	Cat. #: PRB-155P , RRID:AB_292096
TRANCE/TNFSF11/RANKL	R&D Biosystems	Cat. # AF462, RRID:AB_2206198
RANK	R&D Biosystems	Cat. # AF692, RRID:AB_2205357
RANKL	Amgen	Cat. #: M366, PMID: 22711702
RANK	Amgen	Cat. #: N1H8, PMID: 22711702
Keratin 5 (K5)	Fitzgerald	Cat. #: 20R-CP003, RRID:AB_1284039
Keratin 8+18 (K8+18)	Fitzgerald	Cat. #: 20R-CP004, RRID:AB_1284055
SLUG (C19G7)	Cell Signaling Technology	Cat. #: 9585, RRID:AB_2239535
ZEB1 (E2G6Y)	Cell Signaling Technology	Cat. #: 70512, https://www.cellsignal.com/datasheet.jsp?productId=70512&images=1)
phospho-PR (S294)	Carol A. Lange Lab, clone 8508, Knutson, T.P., et al. J Hematol Oncol 10, 89 (2017), PMCID: PMC5392969	PMID: 28412963
CD24-PE	BD Biosciences, clone M1/69	Cat, #: 553262, RRID:AB_394741
CD49f -PE-Cy7	BioLegend, clone GoH3	Cat: #: 313621, RRID:AB_2561704
CD31-APC	BioLegend, clone 390	Cat: #: 102409, RRID:AB_312904
CD45-APC	BioLegend, clone 30-F11	Cat: #: 103111, RRID:AB_312976
TER-119-APC	BioLegend, clone TER-119	Cat: #: 116211, RRID:AB_313712
CD61-FITC	BioLegend, clone 2C9.G2 (HMβ3–1)	Cat. #: 104305, RRID:AB_313082
CD24-PE	BioLegend, clone ML5	Cat, #: 311105, RRID:AB_314854

REAGENT or RESOURCE	SOURCE	IDENTIFIER
EPCAM CD326-FITC	Thermo Fischer Scientific, clone VU-1D9	Cat. #: A15755, RRID:AB_2534535
CD31-PE	BioLegend, clone WM59	Cat: #: 303105, RRID:AB_314331
CD45-PE	BioLegend, clone H130	Cat: #: 304007, RRID:AB_314395
CD235a-PE	BD Biosciences, clone GA-R2	Cat: #: 561051, RRID:AB_10563407
CD61-AF647	BioLegend, clone 2C9.G2 (HMβ3–1)	Cat. #: 104313, RRID:AB_2249337
phospho-p44/42 MAPK (ERK1/2)	Cell Signaling Technology	Cat. #: 9101, RRID:AB_331646
p44/42 MAPK (ERK1/2)	Cell Signaling Technology	Cat. #: 9102, RRID:AB_330744
phospho-PR (S294)	Thermo Fischer Scientific	Cat. #: PA5–37472, RRID:AB_2554081
phospho-PR (S294)	Thermo Fischer Scientific	Cat. #: MA1–414, RRID:AB_325316
PR	Santa Cruz Biotechnology, clone H-190	Cat. #: sc-7208, RRID:AB_2164331
PR	Thermo Fischer Scientific, clone hPRa7	Cat. #: MA5–12658, RRID:AB_11000632
NFkB-p65 (D14E12) XP	Cell Signaling Technology	Cat. #: 8242, RRID:AB_10859369
Lamin B1	Abcam	Cat. #: ab16048,, RRID:AB_443298
TruStain FcX (anti-mouse CD16/32)	BioLegend, clone 93	Cat. #: 101319, RRID:AB_1574973
Goat anti-rabbit IgG (H+L) HRP-conjugated	Advansta	R-05072–500
Goat anti-mouse IgG (H+L) HRP-conjugated	Advansta	R-05071–500
Donkey anti-goat IgG HRP-conjugated	Santa Cruz	sc-2020
Goat anti Mouse IgG (H+L) Alexa Fluor 488	Thermo Fisher Scientific	A-11001, RRID:AB_2534069
Goat anti Mouse IgG (H+L) Alexa Fluor 568	Thermo Fisher Scientific	A-11004, RRID:AB_2534072
Goat anti Mouse IgG (H+L) Alexa Fluor 594	Thermo Fisher Scientific	A-11005, RRID:AB_2534073
Goat anti Mouse IgG (H+L) Alexa Fluor 633	Thermo Fisher Scientific	A-21052, RRID:AB_2535719
Goat anti Mouse IgG (H+L) Alexa Fluor 647	Thermo Fisher Scientific	A-21235, RRID:AB_2535804
Goat anti Rabbit IgG (H+L) Alexa Fluor 488	Thermo Fisher Scientific	A-11008, RRID:AB_143165
Goat anti Rabbit IgG (H+L) Alexa Fluor 568	Thermo Fisher Scientific	A-11011, RRID:AB_143157
Goat anti Rabbit IgG (H+L) Alexa Fluor 594	Thermo Fisher Scientific	A-11012, RRID:AB_2534079
Goat anti Rabbit IgG (H+L) Alexa Fluor 633	Thermo Fisher Scientific	A-21070, RRID:AB_2535731
Goat anti Rabbit IgG (H+L) Alexa Fluor 647	Thermo Fisher Scientific	A-21245, RRID:AB_2535813
Goat anti Guinea pig IgG (H+L) Alexa Fluor 488	Thermo Fisher Scientific	A-11073, RRID:AB_2534117
Goat anti Guinea pig IgG (H+L) Alexa Fluor 568	Thermo Fisher Scientific	A-11075, RRID:AB_2534119
Chemicals, peptides, and recombinant proteins		
Phalloidin Alexa Fluor 488	Thermo Fisher Scientific	A12379

REAGENT or RESOURCE	SOURCE	IDENTIFIER
Phalloidin Alexa fluor 647	Thermo Fisher Scientific	A22287
Mouse serum	Jackson Immunoresearch Laboratories	AB_2337194
Rat serum	Jackson Immunoresearch Laboratories	AB_2337141
protease inhibitor cocktail solutions	genDEPOT, Xpert solutions	P3100
Phosphatase inhibitor cocktail solution	genDEPOT, Xpert solutions	P3200
4′,6-diamidino-2-phenylindole (DAPI)	Thermo Fisher Scientific	D1306
Advansta WesternBright ECL HRP substrate	Advansta	K-12045
Direct Red 80	Sigma-Aldrich	365548
Picric acid solution	Sigma-Aldrich	P6744
Weigert's iron hematoxylin	Richard-Allan Scientific	88028
FBS Benchmark	Gemini Bio Products	100–106
GlutaMAX	Gibco	35050–061
DMEM/F-12, no phenol red	Gibco	21041025
DMEM, high glucose	Gibco	11965092
Cell recovery solution	Corning	354253
B27 Supplement	Gibco	17504044
Cholera Toxin from Vibrio cholerae	Sigma	C8052
propidium iodide	ACROS	440300250
Rat tail collagen-1 (High concentration)	Corning	354249
Basement membrane extract Cultrex BME, type 2, Pathclear	R&D Systems	3532–005-02
Human Plasma Fibronectin Purified Protein	Sigma-Aldrich	FC010
Tamoxifen	Cayman Chemical	13258
LY3214996 (Temuterkib)	InvivoChem	V3178
FAK inhibitor (PND-1186)	Chem Scene	1061353–68-1
EGFR inhibitor (Tyrphostin/AG-1478)	Selleck Chem	S2728
Promegestone/R5020	Perkin Elmer	NLP00400
Collagenase A from Clostridium histolyticum	Roche	13560925
Hyaluronidase from bovine testes	Sigma-Aldrich	H3506
Dispase II from *Bacillus polymyxa*	Sigma-Aldrich	D4693
DNAse I from bovine pancreas	Roche	10104159001
TRIZol (Invitrogen)	Thermo Fisher Scientific	15596026
M-MLV reverse transcriptase	Biochain	Z5040002
L-ribose	Chem Impex International	28127
Critical commercial assays		
Ambion mirVana kit	Thermo Fisher Scientific	AM1560
PerfeCTa SYBR Green FastMix	Quantibio	95072–05K
Mouse DuoSet ELISA Kit TRANCE/ RANKL/TNFSF11	R&D Biosystems	DY462

REAGENT or RESOURCE	SOURCE	IDENTIFIER
NE-PER Nuclear and Cytoplasmic Extraction Reagents	Thermo Fisher Scientific	78833
ImmPRESS HRP Goat Anti-Mouse IgG Polymer Detection Kit, Peroxidase,	Vector Laboratories	MP-7452
ImmPRESS HRP Goat Anti- Rabbit IgG Polymer Detection Kit, Peroxidase,	Vector Laboratories	MP-7451
ImmPACT DAB Substrate Peroxidase	Vector Laboratories	SK-4105
Deposited data		
Source dataset with whole membrane images and FACS gating strategies	Mendeley Data	Northey, Jason (2023), "Cell Stem Cell source data", Mendeley Data, V1, doi: 10.17632/phrmytzyss.1
Experimental models: Cell lines		
T47D	American Type Culture Collection (ATCC)	RRID:CVCL_0553
MCF7	ATCC	RRID:CVCL_0031
Experimental models: Organisms/strains		
V737Nfloxed, FVB/NJ background	UCSF (Weaver lab)	N/A
"KRT5-cre/ERT2" Tg(KRT5-cre/ERT2)1Blh, tm1Sor, C57BL/6J background	UCSF (Rock lab)	RRID:MGI:5304845
"COL" Col1a1tm1Jae, backcrossed more than 10 generations on FVB/NJ background	The Jackson Laboratory	RRID:MGI:3045084 Strain #:002495
"MMTV-PyMT" FVB/N-Tg(MMTV-PyVT)634Mul/J, both FVB/NJ background and C57BL/6J background	UCSF (Werb lab, FVB/NJ) Cold Spring Harbor (Egeblad lab, C57BL/6J)	RRID:IMSR_JAX:002374
"MMTV-Neu" Tg(MMTVneu)202Mul, FVB/NJ background	UCSF (Werb lab)	RRID:MGI:3577096
"Confetti reporter" Gt(ROSA)26Sortm1(CAG-Brainbow2.1)Cle, C57BL/6J background	Cold Spring Harbor (Egeblad lab)	RRID:MGI:4843548
FVB/NJ	The Jackson Laboratory	RRID:IMSR_JAX:001800 Strain #:001800
C57BL/6J	The Jackson Laboratory	RRID:IMSR_JAX:000664 Strain #:000664
V737Nfloxed, FVB/NJ background	UCSF (Weaver lab)	N/A
Oligonucleotides		
Primer: Tnfrsf11a Forward: 5'-ACACCCTGCCTCCTGGGCTT-3'	Asselin-Labat, ML., et al. Nature 465, 798–802 (2010)	N/A
Primer: Tnfrsf11a Reverse: 5'-AAGCCTGGGCCTCCTTGGGT-3'	Asselin-Labat, ML., et al. Nature 465, 798–802 (2010)	N/A
Primer: Ccnd1 Forward: 5'-CCCTGACACCAATCTCCTCAAC-3'	Asselin-Labat, ML., et al. Nature 465, 798–802 (2010)	N/A
Primer: Ccnd1 Reverse: 5'-GCATGGATGGCACAATCTCCA-3'	Asselin-Labat, ML., et al. Nature 465, 798–802 (2010)	N/A
Primer: Ccnd2 Forward: 5'-AGACCTTCATCGCTCTGTGC-3'	Asselin-Labat, ML., et al. Nature 465, 798–802 (2010)	N/A
Primer: Ccnd2 Reverse: 5'-TAGCAGATGACGAACACGCC-3'	Asselin-Labat, ML., et al. Nature 465, 798–802 (2010)	N/A
Primer: Pgr (A+B) Forward: 5'-CGCAGGTTCTCCACACGTC-3'	Joshi, P., et al. Nature 465, 803–807 (2010)	N/A
Primer: Pgr (A+B) Reverse: 5'-GATCGGTATAGGCGAGACTACAGAC-3'	Joshi, P., et al. Nature 465, 803–807 (2010)	N/A

REAGENT or RESOURCE	SOURCE	IDENTIFIER
Primer: Pgr (B) Forward: 5'-CACAGTATGGCTTTGATTCCTTACCTC-3'	Joshi, P., et al. Nature 465, 803–807 (2010)	N/A
Primer: Pgr (B) Reverse: 5'-TGCCCTCTTAAAGAAGACCTTGC-3'	Joshi, P., et al. Nature 465, 803–807 (2010)	N/A
Primer: KRT5 Forward: 5'-CCAAGGTTGATGCACTGATGG-3'	PrimerBank (https://pga.mgh.harvard.edu/primerbank/)	Primer Bank #119395753c1
Primer: KRT5 Reverse: 5'-TGTCAGAGACATGCGTCTGC-3'	PrimerBank (https://pga.mgh.harvard.edu/primerbank/)	Primer Bank #119395753c1
Primer: TNFRSF11B (OPG) Forward: 5'-GCGCTCGTGTTTCTGGACA-3'	PrimerBank (https://pga.mgh.harvard.edu/primerbank/)	Primer Bank #148743792c1
Primer: TNFRSF11B (OPG) Reverse: 5'-AGTATAGACACTCGTCACTGGTG-3'	PrimerBank (https://pga.mgh.harvard.edu/primerbank/)	Primer Bank #148743792c1
Primer: WNT4 Forward: 5'-AGGAGGAGACGTGCGAGAAA-3'	PrimerBank (https://pga.mgh.harvard.edu/primerbank/)	Primer Bank #156630997c1
Primer: WNT4 Reverse: 5'-CGAGTCCATGACTTCCAGGT-3'	PrimerBank (https://pga.mgh.harvard.edu/primerbank/)	Primer Bank #156630997c1
Primer: Yap1 Forward: 5'-ACCCTCGTTTTGCCATGAA-3'	PrimerBank (https://pga.mgh.harvard.edu/primerbank/)	Primer Bank #15928514a1
Primer: Yap1 Reverse: 5'-TGTGCTGGGATTGATATTCCGTA-3'	PrimerBank (https://pga.mgh.harvard.edu/primerbank/)	Primer Bank #15928514a1
Primer: Sox9 Forward: 5'-CAGCCCCTTCAACCTTCCTC-3'	PrimerBank (https://pga.mgh.harvard.edu/primerbank/)	Primer Bank #165932320c3
Primer: Sox9 Reverse: 5'-TGATGGTCAGCGTAGTCGTATT-3'	PrimerBank (https://pga.mgh.harvard.edu/primerbank/)	Primer Bank #165932320c3
Primer: Wwtr1 (Taz) Forward: 5'-CATGGCGGAAAAAGATCCTCC-3'	PrimerBank (https://pga.mgh.harvard.edu/primerbank/)	Primer Bank #19526914a1
Primer: Wwtr1 (Taz) Reverse: 5'-GTCGGTCACGTCATAGGACTG-3'	PrimerBank (https://pga.mgh.harvard.edu/primerbank/)	Primer Bank #19526914a1
Primer: KRT14 Forward: 5'-TGAGCCGCATTCTGAACGAG-3'	PrimerBank (https://pga.mgh.harvard.edu/primerbank/)	Primer Bank #197313720c1
Primer: KRT14 Reverse: 5'-GATGACTGCGATCCAGAGGA-3'	PrimerBank (https://pga.mgh.harvard.edu/primerbank/)	Primer Bank #197313720c1
Primer: TNFSF11 (RANKL) Forward: 5'-CAACATATCGTTGGATCACAGCA-3'	PrimerBank (https://pga.mgh.harvard.edu/primerbank/)	Primer Bank #197927084c1
Primer: TNFSF11 (RANKL) Reverse: 5'-GACAGACTCACTTTATGGGAACC-3'	PrimerBank (https://pga.mgh.harvard.edu/primerbank/)	Primer Bank #197927084c1
Primer: Krt5 Forward: 5'-TCTGCCATCACCCCATCTGT-3'	PrimerBank (https://pga.mgh.harvard.edu/primerbank/)	Primer Bank #20911031a1
Primer: Krt5 Reverse: 5'-CCTCCGCCAGAACTGTAGGA-3'	PrimerBank (https://pga.mgh.harvard.edu/primerbank/)	Primer Bank #20911031a1
Primer: TNFRSF11A (RANK) Forward: 5'-CACCAAATGAACCCCATGTTTAC-3'	PrimerBank (https://pga.mgh.harvard.edu/primerbank/)	Primer Bank #22547111c3
Primer: TNFRSF11A (RANK) Reverse: 5'-GGACTCCTTATCTCCACTTAGGC-3'	PrimerBank (https://pga.mgh.harvard.edu/primerbank/)	Primer Bank #22547111c3
Primer: VIM Forward: 5'-AGTCCACTGAGTACCGGAGAC-3'	PrimerBank (https://pga.mgh.harvard.edu/primerbank/)	Primer Bank #240849334c2
Primer: VIM Reverse: 5'-CATTTCACGCATCTGGCGTTC-3'	PrimerBank (https://pga.mgh.harvard.edu/primerbank/)	Primer Bank #240849334c2
Primer: ZEB2 Forward: 5'-GGAGACGAGTCCAGCTAGTGT-3'	PrimerBank (https://pga.mgh.harvard.edu/primerbank/)	Primer Bank #284413745c2

REAGENT or RESOURCE	SOURCE	IDENTIFIER
Primer: ZEB2 Reverse: 5'-CCACTCCACCCTCCCTTATTTC-3'	PrimerBank (https://pga.mgh.harvard.edu/primerbank/)	Primer Bank #284413745c2
Primer: ZEB1 Forward: 5'-GATGATGAATGCGAGTCAGATGC-3'	PrimerBank (https://pga.mgh.harvard.edu/primerbank/)	Primer Bank #291575187c1
Primer: ZEB1 Reverse: 5'-ACAGCAGTGTCTTGTTGTTGT-3'	PrimerBank (https://pga.mgh.harvard.edu/primerbank/)	Primer Bank #291575187c1
Primer: SNAI1 Forward: 5'-TCGGAAGCCTAACTACAGCGA-3'	PrimerBank (https://pga.mgh.harvard.edu/primerbank/)	Primer Bank #301336132c1
Primer: SNAI1 Reverse: 5'-AGATGAGCATTGGCAGCGAG-3'	PrimerBank (https://pga.mgh.harvard.edu/primerbank/)	Primer Bank #301336132c1
Primer: Sox2 Forward: 5'-GCGGAGTGGAAACTTTTGTCC-3'	PrimerBank (https://pga.mgh.harvard.edu/primerbank/)	Primer Bank #31543759a1
Primer: Sox2 Reverse: 5'-CGGGAAGCGTGTACTTATCCTT-3'	PrimerBank (https://pga.mgh.harvard.edu/primerbank/)	Primer Bank #31543759a1
Primer: SNAI2 Forward: 5'-CGAACTGGACACACATACAGTG-3'	PrimerBank (https://pga.mgh.harvard.edu/primerbank/)	Primer Bank #324072669c1
Primer: SNAI2 Reverse: 5'-CTGAGGATCTCTGGTTGTGGT-3'	PrimerBank (https://pga.mgh.harvard.edu/primerbank/)	Primer Bank #324072669c1
Primer: KRT8 Forward: 5'-CAGAAGTCCTACAAGGTGTCCA-3'	PrimerBank (https://pga.mgh.harvard.edu/primerbank/)	Primer Bank #372466576c1
Primer: KRT8 Reverse: 5'-CTCTGGTTGACCGTAACTGCG-3'	PrimerBank (https://pga.mgh.harvard.edu/primerbank/)	Primer Bank #372466576c1
Primer: KRT18 Forward: 5'-GGCATCCAGAACGAGAAGGAG-3'	PrimerBank (https://pga.mgh.harvard.edu/primerbank/)	Primer Bank #40354194c1
Primer: KRT18 Reverse: 5'-ATTGTCCACAGTATTTGCGAAGA-3'	PrimerBank (https://pga.mgh.harvard.edu/primerbank/)	Primer Bank #40354194c1
Primer: Wnt4 Forward: 5'-AGACGTGCGAGAAACTCAAAG-3'	PrimerBank (https://pga.mgh.harvard.edu/primerbank/)	Primer Bank #6678595a1
Primer: Wnt4 Reverse: 5'-GGAACTGGTATTGGCACTCCT-3'	PrimerBank (https://pga.mgh.harvard.edu/primerbank/)	Primer Bank #6678595a1
Primer: Esr1 Forward: 5'-CCTCCCGCCTTCTACAGGT-3'	PrimerBank (https://pga.mgh.harvard.edu/primerbank/)	Primer Bank #6679695a1
Primer: Esr1 Reverse: 5'-CACACGGCACAGTAGCGAG-3'	PrimerBank (https://pga.mgh.harvard.edu/primerbank/)	Primer Bank #6679695a1
Primer: Krt18 Forward: 5'-CGAGGCACTCAAGGAAGAAC-3'	This paper	N/A
Primer: Krt18 Reverse: 5'-CTTGGTGGTGACAACTGTGG-3'	This paper	N/A
Primer: Ctnnb1 Forward: 5'-GTGGACCCCAAGCCTTAGTA-3'	This paper	N/A
Primer: Ctnnb1 Reverse: 5'-AGTCGCTGACTTGGGTCTGT-3'	This paper	N/A
Primer: Gapdh Forward: 5'-GGGTGTGAACCACGAGAAAT-3'	This paper	N/A
Primer:Gapdh Reverse: 5'-GTCTTCTGGGTGGCAGTGAT-3'	This paper	N/A
Primer: Cdh1 Forward: 5'-TTGGCGTTTTCATCATTGAG-3'	This paper	N/A
Primer: Cdh1 Reverse: 5'-AAAGACCGGCTGGGTAAACT-3'	This paper	N/A

REAGENT or RESOURCE	SOURCE	IDENTIFIER
Primer: Smarca2 Forward: 5'-TCTTGCTGAGCACAAGAGCA-3'	This paper	N/A
Primer: Smarca2 Reverse: 5'-TCTGATCCACGTTCAGCTTG-3'	This paper	N/A
Primer: Snai1 Forward: 5'-AGCCCAACTATAGCGAGCTG-3'	This paper	N/A
Primer: Snai1 Reverse: 5'-GGGGTACCAGGAGAGAGTCC-3'	This paper	N/A
Primer: Snai2 Forward: 5'-GAAGCCCAACTACAGCGAAC-3'	This paper	N/A
Primer: Snai2 Reverse: 5'-GCCCCAAGGATGAGGAGTAT-3'	This paper	N/A
Primer: Zeb1 Forward: 5'-CTGCCCAGTTACCCACAATC-3'	This paper	N/A
Primer: Zeb1 Reverse: 5'-GGCGTGGAGTCAGAGTCATT-3'	This paper	N/A
Primer: Zeb2 Forward: 5'-ACCCAGGACTGGATCAGATG-3'	This paper	N/A
Primer: Zeb2 Reverse: 5'-TCACATGCATACATGCCACTT-3'	This paper	N/A
Primer: Smarca4 Forward: 5'-TGCCTCAGGGAAATTTGAAC-3'	This paper	N/A
Primer: Smarca4 Reverse: 5'-TTCTGCTTTTGTGGTTCCATC-3'	This paper	N/A
Primer: Fn1 Forward: 5'-GTACAATGTGGGACCCTTGG-3'	This paper	N/A
Primer: Fn1 Reverse: 5'-CCTCGGTGTTGTAAGGTGGA-3'	This paper	N/A
Primer: Bmi1 Forward: 5'-GGTACTTACGATGCCCAGCA-3'	This paper	N/A
Primer: Bmi1 Reverse: 5'-CCATCCCTCTGGTGACTCAT-3'	This paper	N/A
Primer: Vim Forward: 5'-AGAGAGAGGAAGCCGAAAGC-3'	This paper	N/A
Primer: Vim Reverse: 5'-AGTGAGGTCAGGCTTGGAAA-3'	This paper	N/A
Primer: Tnfsf11 Forward: 5'-TTAGCATTCAGGTGTCCAACC-3'	This paper	N/A
Primer: Tnfsf11 Reverse: 5'-CGTGGGCCATGTCTCTTAGTA-3'	This paper	N/A
Primer: 18S rRNA (mouse) Forward: 5'-GGATGCGTGCATTTATCAGA-3'	This paper	N/A
Primer: 18S rRNA (mouse) Reverse: 5'-GGCGACTACCATCGAAAGTT-3'	This paper	N/A
Primer: 18S rRNA (human) Forward: 5'-CGGCTACCACATCCAAGGAA-3'	This paper	N/A
Primer: 18S rRNA (human) Reverse: 5'-GCTGGAATTACCGCGGCT-3'	This paper	N/A
Primer: GAPDH Forward: 5'-CGACCACTTTGTCAAGCTCA-3'	This paper	N/A

REAGENT or RESOURCE	SOURCE	IDENTIFIER
Primer: GAPDH Reverse: 5'-AGGGGAGATTCAGTGTGGTG-3'	This paper	N/A
Primer: CDH1 Forward: 5'-GCTGCTCTTGCTGTTTCTTCG-3'	This paper	N/A
Primer: CDH1 Reverse: 5'-AGATACCGGGGGACACTCAT-3'	This paper	N/A
Recombinant DNA		
CNA-35-GFP	Addgene	RRID:Addgene_61603
Software and algorithms		
FlowJo version 10.9.0	FlowJo™	RRID:SCR_008520
IGOR Pro version 6.22A	WaveMetrics, Lake Oswego, OR	RRID:SCR_000325
Image J (FIJI) version 2.14.0/1.54f	NIH	RRID:SCR_003070
QuPath version 0.4.3	(Queen's University Belfast) https://qupath.github.io/	RRID:SCR_018257
GraphPad Prism version 10.0.2	GraphPad Software, LLC	RRID:SCR_002798
Leica Application Suite (LAS) software verstion 4.13	Leica Microsystems	RRID:SCR_016555
BD FACSDiva software version 9.0	BD Biosciences	RRID:SCR_001456
GeneSys software version 1.8.8	Syngene	RRID:SCR_015770
Micro-Manager 2.0.0	(UCSF) NIH	RRID:SCR_000415
NIS Elements software version 5.41.02	Nikon Instruments Inc.	RRID:SCR_014329
MetaMorph Microscopy Automation and Image Analysis Software version 7.10.4	Molecular Devices	RRID:SCR_002368
STIFMap	(in house) https://github.com/cstashko/STIFMaps	
Other		
Immobilon P Polyvinylidene difluoride membrane (PVDF)	Millipore	IPVH00010
8-well chamber slides	LabTek II	154534
Silicon nitride cantilevers (spring constant of 0.06 N m−1) with borosilicate glass spherical tip (5μm diameter)	Novascan Technologies	PT.GS
ZEISS Axio Scan.Z1 digital slide scanner	ZEISS	RRID:SCR_020927
Leica TCS SP5 (five channels) Confocal Microscope	Leica	RRID:SCR_020233
Eppendorf realplex2 epgradient S mastercycler	Eppendorph	N/A
Olympus microscope (IX81) fitted with an analyser (U-ANT) and a polarizer (U-POT, Olympus) oriented parallel and orthogonal to each other	Olympus	RRID:SCR_020341
Inverted Eclipse Ti Nikon microscope with CSU-X1 spinning disk confocal (Yokogawa Electric Corporation), 405 nm, 488 nm, 561, 635 nm lasers, Plan Apo VC 60X/1.40 Oil or an Apo LWD 40X/1.15 Water-immersion lS objective; electronic shutters; a charge-coupled device (CCD) camera (Clara; Andor) and controlled by Metamorph	Nikon Instruments Inc.	RRID:SCR_021242

REAGENT or RESOURCE	SOURCE	IDENTIFIER
Nikon Ti-E Microscope (Inverted) with CSU-W1 widefield spinning disk confocal (Andor Borealis), 100 mW at 405, 561, and 640 nm; 150 mW at 488 nm lasers, an Andor Zyla sCMOS camera (5.5 megapixels) and Andor iXon Ultra DU888 1k x 1k Electron multiplying CCD to enable large field of view confocal imaging and controlled by Micromanager	Nikon Instruments Inc.	RRID:SCR_021242
Nikon SoRa Spinning Disk microscope controlled by NIS Elements software	Nikon Instruments Inc.	N/A
BD FACS Aria II cell sorters	BD Biosciences	RRID:SCR_018091
MFP3D-BIO inverted optical AFM (Asylum Research, Santa Barbara, CA) mounted on a Nikon TE200-U inverted microscope (Melville, NY) and placed on a vibration-isolation table (Herzan TS-150)	Oxford Instruments, Asylum research	RRID:SCR_020366
PXi4 imaging system (gel documentation)	SynGene	N/A